8-2019

Electrostatically Actuated Double Wall Carbon Nanotubes to Include Intertube van der Waals Forces

Ezequiel Juarez Ocanas
The University of Texas Rio Grande Valley

ELECTROSTATICALLY ACTUATED DOUBLE WALL CARBON NANOTUBES TO INCLUDE INTERTUBE VAN DER WAALS FORCES

A Thesis

by

EZEQUIEL JUAREZ OCANAS

Submitted to the Graduate College of
The University of Texas Rio Grande Valley
In partial fulfillment of the requirements for the degree of

MASTER OF SCIENCE IN ENGINEERING

August 2019

Major Subject: Mechanical Engineering

ELECTROSTATICALLY ACTUATED DOUBLE WALL CARBON NANOTUBES TO INCLUDE INTERTUBE VAN DER WAALS FORCES

A Thesis
by
EZEQUIEL JUAREZ OCANAS

COMMITTEE MEMBERS

Dr. Dumitru Caruntu
Chair of Committee

Dr. Dorina Chipara
Committee Member

Dr. Nazmul Islam
Committee Member

Dr. Mataz Alcoutlabi
Committee Member

August 2019

ABSTRACT

Juarez Ocanas, Ezequiel, Electrostatically Actuated Double Wall Carbon Nanotubes to Include Intertube van der Waals Forces. Master of Science Engineering (MSE), August, 2019, 58 pp., 8 tables, 32 figures, references, 39 titles.

This work deals with the amplitude-frequency and amplitude-voltage responses of parametric and primary resonances of electrostatically actuated double-walled carbon nanotubes (DWCNTs). Nonlinear forces acting on the DWCNT are intertube van der Waals and electrostatic forces. Soft AC excitation and small viscous damping are assumed. In coaxial vibration, the outer and inner carbon nanotubes move together (in-phase), maintaining their geometric concentricity; while in noncoaxial vibration, the CNTs move in opposite direction (out-of-phase). Modal coordinate transformation is formulated. The Harmonic Balance Method (HBM) is used to find the free response solutions of the DWCNT. The Reduced Order Model (ROM) method is also used in this investigation. All ROMs using one through five modes of vibration (terms) are developed in terms of modal coordinates. ROM using one term is solved and frequency-amplitude response predicted by using the Method of Multiple Scales (MMS). All models and methods are in agreement at lower amplitudes for coaxial vibration, while in higher amplitudes only ROM with five terms provides reliable results. The effects of voltage, detuning frequency, and damping on the various resonance responses of electrostatically actuated DWCNTs are reported. A discussion of stability and bifurcation analysis is presented.

DEDICATION

I dedicate my thesis to my wife, Angela Nino, and my son, Sebastian Juarez. This work would not have been possible without your constant support and motivation. Thank you for your love and patience.

ACKNOWLEDGMENT

I am thankful to Dr. Dumitru Caruntu, chair of my thesis committee, for his mentorship. Thank you for your constant advice and encouragement throughout my time as a graduate research student. This work would not have been possible without your guidance and support. Your many life lessons have inspired me to become a better engineer. I am also grateful for my thesis committee members, Drs. Dorina Chipara, Nazmul Islam, and Mataz Alcoutlabi, for their valuable feedback and encouragement.

TABLE OF CONTENTS

Page

LIST OF FIGURES

Page

LIST OF TABLES

Page

CHAPTER I

INTRODUCTION

In 1991, Sumio Iijima discovered the fullerene-based carbon nanotube (CNT) [1]. CNTs [2] are known for their excellent mechanical, electrical, and chemical properties that warrant further research in the field of nanoelectromechanical systems (NEMS). DWCNTs, the simplest type of multi-walled carbon nanotubes (MWCNTs), are comprised of exactly two concentric CNTs, one tube nested within the other. Applications of DWCNTs may be seen in the areas of lasers [3-5], sensors [6-10], and transistors and switches [11-12]. In applications of DWCNTs as resonator sensors for mass sensing, electrostatic actuation is commonly used. Pull-in instability is a phenomenon that occurs in systems under electrostatic actuation [13]. Free vibration response of DWCNTs has been previously reported [14]. For these cases, coaxial vibration has been considered.

Yan et al. [15] employed the concept of nonlinear normal modes (NNMs) to model the nonlinear dynamical behavior of DWCNTs. They used a continuum elastic beam model devoid of damping and external forces with an intent to focus on free vibration. They investigated the case of internal resonance and the case of no internal resonance using the method of multiple scales (MMS) to approximate the solutions of the NNMs. They concluded that, in the coaxial mode of vibration, the inner and outer carbon nanotube vibrate with an amplitude ratio that is "very close to unity". Natsuki et al. [16] also used a continuum Euler-Bernoulli beam model to characterize DWCNTs of varying lengths of inner and outer carbon nanotubes, and under free

vibration. They investigated the natural frequencies of a DWCNT up to the seventh mode of vibration and concluded that vibrational frequencies decrease when the length of either the inner or outer carbon nanotube is increased while the other is kept constant. The utility of controlling the lengths of the inner and outer carbon nanotubes of DWCNTs is that they may operate at different frequencies as desired.

Murmu et al. [17] used nonlocal Euler-Bernoulli beam theory to model a DWCNT subjected to an axial magnetic field. Their analytical solutions were for natural frequencies of the DWCNTs under a magnetic field. They concluded that for both coaxial and noncoaxial modes of vibrations, the presence of the longitudinal magnetic field increases the natural frequencies. Hajnayeb and Khadem [18] modeled DWCNTs using Euler-Bernoulli beam theory to include linear damping, stretching terms, nonlinear intertube van der Waals, and nonlinear electrostatic forces. They applied a perturbation method and long-time integration method to approximate for solutions for the amplitude-frequency response under primary and secondary resonance conditions. They concluded that, like single-walled carbon nanotubes (SWCNTs), DWCNTs experienced softening and hardening behavior depending on the value of DC voltage. Additionally, they remarked that when the AC frequency is at either the coaxial or noncoaxial frequency, the other mode is "damped out in the steady-state response because of system damping". Hudson and Sinha [19] applied order reduction methods (modal domain analysis (MDA) and modified modal domain analysis (MMDA)) in atomistic simulations to investigate the effects of defects on the vibrational behavior of carbon nanotubes. They concluded that, compared to MDA, MMDA results in a "valid and useful approximation of the perturbed system" and both are suitable tools for investigation of high degree-of-freedom systems.

In this thesis, the amplitude-frequency and amplitude-voltage responses of parametric and primary resonances of cantilevered DWCNTs under soft Alternating Current (AC) electrostatic actuation is investigated. The AC frequency is near (and near-half) the first coaxial natural frequency for parametric (and primary) resonance. The electrostatic and intertube van der Waals forces are the nonlinear forces. Reduced order models (ROMs) [20-21] of up to five modes of vibration (terms) are used to transform the partial differential equation of motion into a system of ordinary differential equations. The ROM using one mode of vibration is solved using the method of multiple scales (MMS) [22]. In the analytical solution of MMS, the equations are coupled by the intertube van der Waals force. A Taylor polynomial is used to approximate the nonlinear electrostatic force per unit length. The equations of motion are decoupled in their linear part by using modal coordinates. These coordinates are then used for the nonlinear problem, and the amplitude-frequency and amplitude-voltage responses of the DWCNT coaxial vibrations are reported. Also, numerical integrations of ROMs using two, three, four, and five modes of vibration are utilized to investigate the parametric and primary resonance of coaxial vibrations of DWCNTs. The effects of voltage, detuning frequency, and damping parameters on the DWCNT resonant responses are reported.

CHAPTER II

DIFFERENTIAL EQUATIONS OF MOTION

Euler-Bernoulli elastic beam model, valid for structures with high length-to-diameter ratio [23], is used in this work. The model of DWCNTs, Fig. 1, accounts for electrostatic, damping, and intertube van der Waals forces.

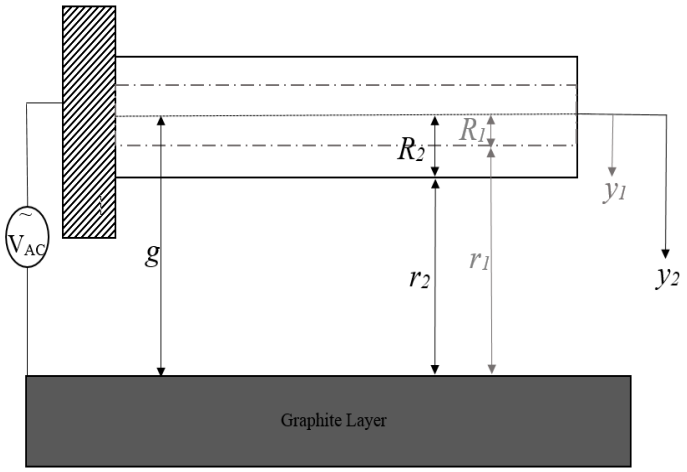

Fig. 1. DWCNT cantilever under electrostatic, damping and van der Waals forces.

The governing partial differential equations of motion are given by

$$\rho A_1 \frac{\partial^2 y_1}{\partial t^2} + EI_1 \frac{\partial^4 y_1}{\partial x^4} = f_{vdWT-T} \tag{1}$$

$$\rho A_2 \frac{\partial^2 y_2}{\partial t^2} + EI_2 \frac{\partial^4 y_2}{\partial x^4} = -b\frac{\partial y_2}{\partial t} - f_{vdWT-T} + f_{elec} \tag{2}$$

where $y_1(x,t)$ and $y_2(x,t)$ are the deflections of inner and outer CNTs, respectively, A_1 and A_2 cross-sectional areas, I_1 and I_2 cross-sectional moments of inertia, x axial longitudinal coordinate, t time, ρ density, and b damping per unit length coefficient. The forces acting on the

DWCNT are given at the right side of Eqs. (1) and (2). The forces are: damping, due to viscosity, intertube van der Waals f_{vdWT-T}, and electrostatic force f_{elec}. The subscripts n = 1, 2 in Eqs. (1) and (2) represent the inner and outer tube, respectively.

Due to the presence of a viscous (air) environment, the damping force must be taken into account when modeling the DWCNT. Since the viscous fluid comes in direct contact with the outer tube, the damping is assumed to be acting only on the outer tube. Damping is considered to be proportional to the velocity of the tube as follows $f_{damp} = b \cdot \partial y_2 / \partial t$. Bhiladvala and Wang [24] provide a linear, fluid damping model that relates pressure and temperature to the fluid damping coefficient. A dry air medium under a pressure of 110 Pa (medium vacuum) and temperature of 300 K (room temperature) is considered. The values for the physical constants and dry air conditions for fluid damping afterwards numerical simulations may be found in Tables 1 and 2.

Table 1. Physical Constants [25]

Symbol	*Description*	*Value (unit)*
ε_0	Permittivity of vacuum	$8.85 \cdot 10^{-12}$ [$C^2/N/m^2$]
E	Young modulus	$1.0 \cdot 10^{12}$ [N/m^2]
C_1	VdW interlayer coefficient	$71.11 \cdot 10^{9}$ [N/m^2]
C_3	VdW interlayer coefficient	$2.57 \cdot 10^{31}$ [N/m^4]
ρ	Mass density	$2.3 \cdot 10^{3}$ [kg/m^3]
K_B	Boltzmann Constant	$1.38064852 \cdot 10^{-23}$ [m^2 kg/ (s^2 K)]
N	Avogadros Number	$6.022140857 \cdot 10^{23}$ [mol^{-1}]

Table 2. Fluid Damping Conditions (Dry Air)

Symbol	*Description*	*Value (unit)*
P	Absolute Pressure	110 [Pa]
R	Specific Gas Constant for Dry Air	287.05 [$m^2/(s^2$ K)]
T	Absolute Temperature	300 [K]
d	Mean Diameter of Air Molecule	$0.3 \cdot 10^{-9}$[m]
M_m	Molecular Mass of Dry Air	0.02897 [kg/mol]

The intertube force f_{vdWT-T} provides the coupling that introduces the two modes of vibration of a DWCNT: coaxial (in-phase CNTs) and noncoaxial (180^o out-of-phase CNTs). A Taylor polynomial describes the intertube van der Waals force as follows [25]:

$$f_{vdWT-T} = C_1(y_2 - y_1) + C_3(y_2 - y_1)^3 \tag{3}$$

where C_1 is van der Waals interlayer interaction coefficient of the linear term, and C_3 is van der Waals interlayer interaction coefficient of the cubic term.

Using a standard capacitance model of a multi-walled carbon nanotube [13, 26] and assuming that all charges dominate and are applied only on the outer carbon nanotube due to the Faraday Cage Effect [27], the electrostatic force per unit length is given by [2,13]:

$$f_{elec} = \frac{\pi\varepsilon_0 V^2}{R_2\sqrt{\frac{\hat{r}_2(\hat{r}_2+2R_2)}{R_2^{\,2}}}\ln^2\left[1+\frac{\hat{r}_2}{R_2}+\sqrt{\frac{\hat{r}_2(\hat{r}_2+2R_2)}{R_2^{\,2}}}\right]} \tag{4}$$

where ε_0 is permittivity of vacuum, R_2 is the radius of the conducting outer tube, and $\hat{r}_2$ is the distance from the ground plate (graphite sheet) to the bottom of the outer carbon nanotube, Fig. 1. The *AC* voltage is given by

$$V = V_0\cos\Omega t \tag{5}$$

where V_0 and Ω are the amplitude and circular frequency of the *AC* voltage, respectively. The gap g, see Table 3, is the distance from the graphite sheet to the center of the DWCNT, Fig. 1, and it is given by:

$$g = y_2 + R_2 + \hat{r}_2 \tag{6}$$

Consider the following dimensionless variables:

$$w_n = \frac{y_n}{g}\ ;\ z = \frac{x}{\ell}\ \ ;\ \ \tau = \frac{t}{\ell^2}\sqrt{\frac{EI_2}{\rho A_2}} \tag{7}$$

where n = 1,2, ℓ is the length of the DWCNT and R_{eq} is the equilibrium interlayer spacing, see Table 3; w, z, and τ are dimensionless deflection, dimensionless longitudinal coordinate, and dimensionless time, respectively; and y, x, and t are their corresponding dimensional variables. Substituting Eq. (7) into Eqs. (1) and (2), the following system of dimensionless partial differential equations of motion result:

$$\begin{cases} A^* \dfrac{\partial^2 w_1}{\partial \tau^2} + I^* \dfrac{\partial^4 w_1}{\partial z^4} = \overline{f}_{vdWT-T} \\ \dfrac{\partial^2 w_2}{\partial \tau^2} + \dfrac{\partial^4 w_2}{\partial z^4} = -b^* \dfrac{\partial w_2}{\partial \tau} - \overline{f}_{vdWT-T} + \delta \overline{f}_{elec} \cos^2 \Omega^* \tau \end{cases} \tag{8}$$

where the dimensionless intertube van der Waals force $\overline{f}_{vdWT-T}$ and electrostatic force $\overline{f}_{elec}$ are given by

$$\overline{f}_{vdWT-T} = C_1^*(w_2 - w_1) + C_3^*(w_2 - w_1)^3 \tag{9}$$

$$\overline{f}_{elec} = \left[(1-w_2)^2 - s_2{}^2\right]^{-\frac{1}{2}} \ln^{-2}\left(\frac{1-w_2}{s_2} + \sqrt{\frac{(1-w_2)^2}{s_2^2} - 1}\right) \tag{10}$$

and $s_2 = R_2 / g$. The dimensionless electrostatic force Eq. (10) is approximated using a Taylor polynomial as follows:

$$\overline{f}_{elec}(w_2) = \sum_{k=0}^{3} \alpha_k w_2{}^k \tag{11}$$

Dimensionless area A^*, dimensionless moment of inertia I^*, dimensionless coefficients C_1^* and C_3^* of linear and cubic terms of intertube van der Waals force, dimensionless damping b^*, dimensionless voltage parameter δ, and dimensionless actuation frequency Ω^* of Eq. (8) are given by:

$$A^* = \frac{A_1}{A_2},\ I^* = \frac{I_1}{I_2},\ C_1^* = \frac{C_1 \ell^4}{EI_2},\ C_3^* = \frac{C_3 g^2 \ell^4}{EI_2}$$
$$\delta = \frac{\pi \varepsilon_0 \ell^4 V_0^2}{EI_2 g^2},\ \Omega^* = \Omega \ell^2 \sqrt{\frac{\rho A_2}{EI_2}},\ b^* = \frac{b\ell^2}{\sqrt{\rho A_2 EI_2}} \tag{12}$$

Tables 1 and 3 give the values of the physical constants and dimensional parameters of the DWCNT used for the afterwards numerical simulations.

Table 3. Dimensional Parameters of the System [13]

Symbol	*Description*	*Value (unit)*
ℓ	Length of CNT	$200 \cdot 10^{-9}$ [m]
R_1	Inner tube radius	$0.35 \cdot 10^{-9}$ [m]
R_2	Outer tube radius	$0.70 \cdot 10^{-9}$ [m]
R_{eq}	Interlayer Equilibrium Spacing	$0.34146 \cdot 10^{-9}$[m]
h	Effective Thickness	$0.34 \cdot 10^{-9}$ [m]
g	Gap CNT-plate	$50 \cdot 10^{-9}$ [m]

The areas and moments of inertia are calculated as follows, Fig. 2:

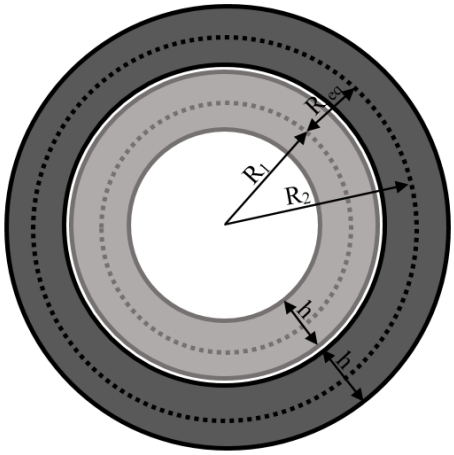

Fig. 2. DWCNT Cross Section.

$$A_i = \pi\left[(R_i + h/2)^2 - (R_i - h/2)^2\right] \tag{13}$$

$$I_i = \frac{\pi}{4}\left[(R_i + h/2)^4 - (R_i - h/2)^4\right] \tag{14}$$

where i = 1,2, and h is the effective thickness of each tube in the DWCNT.

CHAPTER III

MODAL COORDINATE TRANSFORMATION

The two concentric CNTs are coupled through the intertube van der Waals force. Only the linear expression is considered for the decoupling, wherein the new *r*-coordinate (modal) system will be applied to the nonlinear terms. Consider the following DWCNT system under free vibration with only the linear van der Waals force being applied:

$$\begin{cases} A^* \dfrac{\partial^2 w_1}{\partial \tau^2} + I^* \dfrac{\partial^4 w_1}{\partial z^4} = -C_1^*(w_1 - w_2) \\ \dfrac{\partial^2 w_2}{\partial \tau^2} + \dfrac{\partial^4 w_2}{\partial z^4} = C_1^*(w_1 - w_2) \end{cases} \tag{15}$$

Assume the deflections as follows:

$$w_1 = u_1(\tau)\phi_1(z)\,;\; w_2 = v_1(\tau)\phi_1(z) \tag{16}$$

where $\phi(z)$ is the first cantilever mode shape, and u_1 and v_1 are functions of time of the inner and outer tube, respectively. Assume

$$u_1(\tau) = A\cos\omega_{1I}\tau\,;\; v_1(\tau) = B\cos\omega_{1O}\tau \tag{17}$$

where *A*, ω_{1I}, and *B*, ω_{1O} are the amplitudes and natural frequencies of the inner and outer tube, respectively. To find the coaxial natural frequencies of the CNTs, the right sides of Eqs. (15), i.e. the linear van der Waals forces, are equated to zero. Substituting Eqs. (16) and (17) into Eq. (15) yields the following:

$$\begin{cases} I^{*}\phi^{(4)}(z) = A^{*}{\omega_{1I}}^{2}\phi(z) \\ \phi^{(4)}(z) = {\omega_{1O}}^{2}\phi(z) \end{cases} \tag{18}$$

From Eq. (18), the following relationship can be established:

$${\omega_{1O}}^{2} = \frac{A^{*}}{I^{*}}{\omega_{1I}}^{2} \tag{19}$$

Substituting Eqs. (16-19) into Eq. (15) yields the following system of second order ordinary differential equations:

$$\begin{cases} A^{*}\ddot{u}_1 + A^{*}{\omega_{1I}}^{2}u_1 = C_1^{*}(v_1 - u_1) \\ \ddot{v}_1 + {\omega_{1O}}^{2}v_1 = C_1^{*}(u_1 - v_1) \end{cases} \tag{20}$$

Equation (20) is rewritten as follows:

$$M\begin{bmatrix} \ddot{u}_1 \\ \ddot{v}_1 \end{bmatrix} + K\begin{bmatrix} u_1 \\ v_1 \end{bmatrix} = \begin{bmatrix} 0 \\ 0 \end{bmatrix} \tag{21}$$

where ***M*** is the mass matrix and ***K*** is the stiffness matrix. ***M*** and ***K*** are as follows:

$$M = \begin{bmatrix} A^{*} & 0 \\ 0 & 1 \end{bmatrix} \quad , \quad K = \begin{bmatrix} C_1^{*} + A^{*}{\omega_{1I}}^{2} & -C_1^{*} \\ -C_1^{*} & C_1^{*} + {\omega_{1O}}^{2} \end{bmatrix} \tag{22}$$

The mass-normalized stiffness matrix is given by [28]:

$$\tilde{K} = M^{-\frac{1}{2}}KM^{-\frac{1}{2}} \tag{23}$$

Solving the symmetric eigenvalue problem *det($\tilde{K}$ -λ I)* yields λ_1, λ_2 and $\boldsymbol{V_1}$, $\boldsymbol{V_2}$, the eigenvalues and eigenvectors of the system, respectively. Note that $I\begin{bmatrix} \ddot{u}_1 & \ddot{v}_1 \end{bmatrix}^T + \tilde{K}\begin{bmatrix} u_1 & v_1 \end{bmatrix}^T = 0$. The ***P***-matrix is constructed as follows:

$$P = \begin{bmatrix} V_1 & V_2 \end{bmatrix} \tag{24}$$

Matrix ***S*** that transforms the coordinate system from the *u*-coordinates to modal *r*-coordinates, is given by

$$S = M^{-\frac{1}{2}} P \tag{25}$$

Therefore, the modal coordinate transformation for the DWCNT system is given by ***u*** = ***Sr,*** and it can be written as follows:

$$\begin{bmatrix} u_1 \\ v_1 \end{bmatrix} = \begin{bmatrix} c & d \\ e & f \end{bmatrix} \begin{bmatrix} r_1 \\ r_2 \end{bmatrix} \tag{26}$$

where *c, d, e,* and *f* are components of the matrix ***S.*** These values have been calculated using the Matlab function *eig* of the mass-normalized stiffness matrix. They are given in Table 4.

Table 4. Coordinate Transformation Constants

Symbol	*Value*
c	0.81649
d	1.15470
e	0.81649
f	-0.57735

Using Eq. (26), Eq. (7) becomes:

$$\ddot{r} + \Lambda r = P^T M^{-\frac{1}{2}} F(r) \ , \quad \Lambda = \begin{bmatrix} \bar{\omega}_1^2 & 0 \\ 0 & \bar{\omega}_2^2 \end{bmatrix} \tag{27}$$

Table 5. Coaxial and noncoaxial natural frequencies.

Symbol	*Value*
$\bar{\omega}_1$	3.07309
$\bar{\omega}_2$	29660.65309

where ***F*** is the column matrix of applied forces of Eqs. (8), $\bar{\omega}_1$, and $\bar{\omega}_2$ are the DWCNT's coaxial and noncoaxial frequencies of resonance, respectively, and $r = \left[r_1 \; r_2 \right]^T$. Moreover ***F(r)*** is the column matrix *F* of the applied forces after the substitution of modal coordinate transformation given by Eq. (26). To be able to use Eq. (27) with nonlinear terms, Eq. (16) is substituted into Eq. (8) which is then multiplied by the operator $\int_0^1 \bullet \, \phi(z) dz$. The following coefficients result:

$$g_k = \int_0^1 \phi^{k+1}(z) dz \tag{28}$$

These coefficients have been previously calculated by Caruntu and Knecht [29], Table 6.

Table 6. g-coefficients for First Natural Frequency. [29]

Symbol	*Value*
g_0	0.7830
g_1	1.0000
g_2	1.4778
g_3	2.3488

CHAPTER IV

METHOD OF MULTIPLE SCALES

To investigate the parametric resonance of DWCNTs, MMS is used to solve the *r*-coordinate system of differential equations where solutions of zero and first order problems may be found more readily. Consider b^* and δ to be small, i.e. the system is under soft excitation and small damping. The intertube coefficients may not be assumed to be small, in fact they are large coefficients. Setting the small parameters (b^* and δ) to a slow scale time scale by multiplying them by ε, a small dimensionless bookkeeping parameter, Eqs. (27) becomes:

$$\begin{cases} \ddot{r}_1 + \bar{\omega}_1^{\,2} r_1 = cC_3^{\,*}\left(er_1 + fr_2 - cr_1 - dr_2\right)^3 g_3 + \\ e\Big[C_3^{\,*}\left(cr_1 + dr_2 - er_1 - fr_2\right)^3 g_3 - \varepsilon b^*(e\dot{r}_1 + f\dot{r}_2) + \\ \varepsilon\delta\sum_{k=0}^{3}\alpha_k g_k (er_1 + fr_2)^k \cos^2\Omega^*\tau \Big] \\ \\ \ddot{r}_2 + \bar{\omega}_2^{\,2} r_2 = dC_3^{\,*}\left(er_1 + fr_2 - cr_1 - dr_2\right)^3 g_3 + \\ f\Big[C_3^{\,*}\left(cr_1 + dr_2 - er_1 - fr_2\right)^3 g_3 - \varepsilon b^*(e\dot{r}_1 + f\dot{r}_2) + \\ \varepsilon\delta\sum_{k=0}^{3}\alpha_k g_k (er_1 + fr_2)^k \cos^2\Omega^*\tau \Big] \end{cases} \tag{29}$$

where the values of coefficients α_k are given in Table 7.

Table 7. Taylor Expansion Coefficients of Eq. (11)

Symbol	*Value*
α_0	0.04062
α_1	0.05700
α_2	0.07016
α_3	0.08193

Consider fast $T_0 = \tau$ and slow $T_1 = \varepsilon\tau$ time scales, and first-order expansions of r_1 and r_2 as follows:

$$\begin{cases} r_1 = r_{10} + \varepsilon r_{11} \\ r_2 = r_{20} + \varepsilon r_{21} \end{cases} \tag{30}$$

where r_{10}, r_{20}, and r_{11}, r_{21} are the zero-order and first-order approximation solutions. The time derivative is then expressed in terms of derivatives with respect to the fast and slow scales:

$$\frac{\partial}{\partial\tau} = D_0 + \varepsilon D_1 \;;\; \frac{\partial^2}{\partial\tau^2} = D_0{}^2 + 2\varepsilon D_0 D_1 \;;\; D_i = \frac{\partial}{\partial T_i} \tag{31}$$

Substituting Eqs. (30) and (31) into Eq. (29), it results:

$$
\begin{cases}
\left(D_0^{\,2}+2\varepsilon D_0D_1\right)\left(r_{10}+\varepsilon r_{11}\right)+\bar{\omega}_1^{\,2}\left(r_{10}+\varepsilon r_{11}\right)= \\
cC_3^{\,*}\left[e\left(r_{10}+\varepsilon r_{11}\right)+f\left(r_{20}+\varepsilon r_{21}\right)-c\left(r_{10}+\varepsilon r_{11}\right)-d\left(r_{20}+\varepsilon r_{21}\right)\right]^3 g_3+ \\
e\left\{C_3^{\,*}\left[c\left(r_{10}+\varepsilon r_{11}\right)+d\left(r_{20}+\varepsilon r_{21}\right)-e\left(r_{10}+\varepsilon r_{11}\right)-f\left(r_{20}+\varepsilon r_{21}\right)\right]^3 g_3-\right. \\
\varepsilon b^*\left[e\left(D_0+\varepsilon D_1\right)\left(r_{10}+\varepsilon r_{11}\right)+f\left(D_0+\varepsilon D_1\right)\left(r_{20}+\varepsilon r_{21}\right)\right]+ \\
\left.\varepsilon\delta\sum_{k=0}^{3}\alpha_k g_k\left[e\left(r_{10}+\varepsilon r_{11}\right)+f\left(r_{20}+\varepsilon r_{21}\right)\right]^k\cos^2\Omega^* T_0\right\} \\
\\
\left(D_0^{\,2}+2\varepsilon D_0D_1\right)\left(r_{20}+\varepsilon r_{21}\right)+\bar{\omega}_2^{\,2}\left(r_{20}+\varepsilon r_{21}\right)= \\
dC_3^{\,*}[e\left(r_{10}+\varepsilon r_{11}\right)+f\left(r_{20}+\varepsilon r_{21}\right)-c\left(r_{10}+\varepsilon r_{11}\right)-d\left(r_{20}+\varepsilon r_{21}\right)]^3 g_3+ \\
f\left\{C_3^{\,*}\left[c\left(r_{10}+\varepsilon r_{11}\right)+d\left(r_{20}+\varepsilon r_{21}\right)-e\left(r_{10}+\varepsilon r_{11}\right)-f\left(r_{20}+\varepsilon r_{21}\right)\right]^3 g_3-\right. \\
\varepsilon b^*\left[e\left(D_0+\varepsilon D_1\right)\left(r_{10}+\varepsilon r_{11}\right)+f\left(D_0+\varepsilon D_1\right)\left(r_{20}+\varepsilon r_{21}\right)\right]+ \\
\left.\varepsilon\delta\sum_{k=0}^{3}\alpha_k g_k\left[e\left(r_{10}+\varepsilon r_{11}\right)+f\left(r_{20}+\varepsilon r_{21}\right)\right]^k\cos^2\Omega^* T_0\right\}
\end{cases}
\tag{32}
$$

From Eq. (32), the following two problems result, the zero-order problem

$$
\varepsilon^0:\begin{cases}
D_0^{\,2}r_{10}+\bar{\omega}_1^{\,2}r_{10}=(c-e)C_3^{\,*}g_3\left(er_{10}+fr_{20}-cr_{10}-dr_{20}\right)^3 \\
D_0^{\,2}r_{20}+\bar{\omega}_2^{\,2}r_{20}=(d-f)C_3^{\,*}g_3\left(er_{10}+fr_{20}-cr_{10}-dr_{20}\right)^3
\end{cases}
\tag{33}
$$

and first-order problem:

$$
\varepsilon^1:\begin{cases}
D_0^{\,2}r_{11}+\bar{\omega}_1^{\,2}r_{11}=-2D_0D_1r_{10}-eb^*\left(eD_0r_{10}+fD_0r_{20}\right)+e\delta\sum_{k=0}^{3}\alpha_k g_k\left(er_{10}+fr_{20}\right)^k\left(\frac{1+\cos 2\Omega^* T_0}{2}\right) \\
D_0^{\,2}r_{21}+\bar{\omega}_2^{\,2}r_{21}=-2D_0D_1r_{20}-fb^*\left(eD_0r_{10}+fD_0r_{20}\right)+f\delta\sum_{k=0}^{3}\alpha_k g_k\left(er_{10}+fr_{20}\right)^k\left(\frac{1+\cos 2\Omega^* T_0}{2}\right)
\end{cases}
\tag{34}
$$

4.1 HARMONIC BALANCE METHOD

In order to solve the zero-order problem, Eqs. (33), consider r_{10} and r_{20} to be as follows:

$$\begin{cases} r_{10} = p(T_1)\left[e^{i\omega T_0} + e^{-i\omega T_0}\right] \\ r_{20} = q(T_1)\left[e^{i\omega T_0} + e^{-i\omega T_0}\right] \end{cases} \tag{35}$$

and use the Harmonic Balance Method (HBM). Substituting Eq. (35) into Eq. (33) and multiplying by $\int_0^{2\pi/\omega} \bullet \cos(\omega t)\, dT_0$ the following system of equations results:

$$\begin{cases} m[(e-c)p + (f-d)q]^3 = \left(\bar{\omega}_1^{\,2} - \omega^2\right) p\mu_1 \\ m[(e-c)p + (f-d)q]^3 = \left(\bar{\omega}_2^{\,2} - \omega^2\right) q\mu_2 \end{cases} \tag{36}$$

where,

$$\begin{aligned} \mu_1 &= \frac{2}{c-e}\int_0^{\frac{2\pi}{\omega}} \cos^2(\omega T_0)\, dT_0 \\ \mu_2 &= \frac{2}{d-f}\int_0^{\frac{2\pi}{\omega}} \cos^2(\omega T_0)\, dT_0 \\ m &= 8C_3^{\,*} g_3 \int_0^{\frac{2\pi}{\omega}} \cos^4(\omega T_0)\, dT_0 \end{aligned} \tag{37}$$

Solving Eq. (36) for amplitudes *p* and *q* yields to the amplitude-frequency response for free vibration by considering Eq. (16), Eq. (26), and Eq. (35) for the tip deflections. Eq. (36) is solved by using substitution method where $p = \left(\bar{\omega}_2^{\,2} - \omega^2\right)\mu_2 \left(\left(\bar{\omega}_1^{\,2} - \omega^2\right)\mu_1\right)^{-1} q$ and graphed in Matlab by setting arrays for ω. Two cases result, coaxial vibrations [25], i.e. the inner and outer tubes move together synchronously with the same amplitude, Fig. 3, and noncoaxial vibrations, i.e. the inner and outer tube move in opposite phase, Fig. 4.

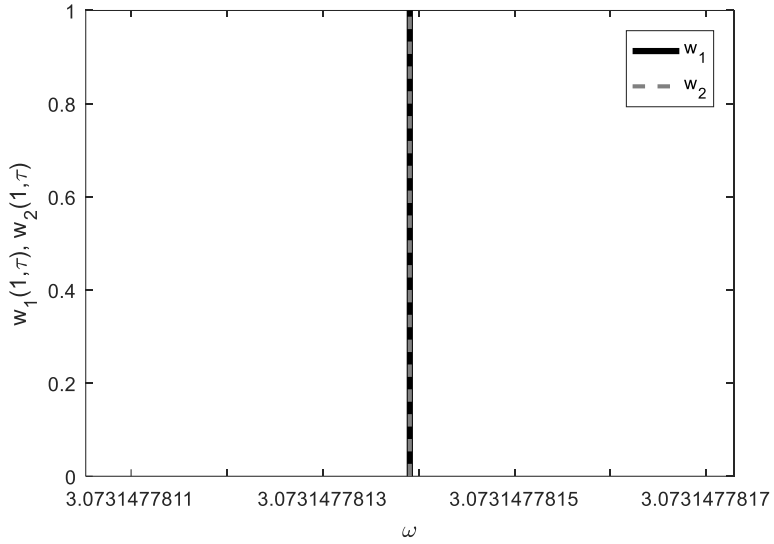

Fig. 3. Free response (g = 1) of the coaxial vibrational mode of the free end z = 1 of DWCNT.

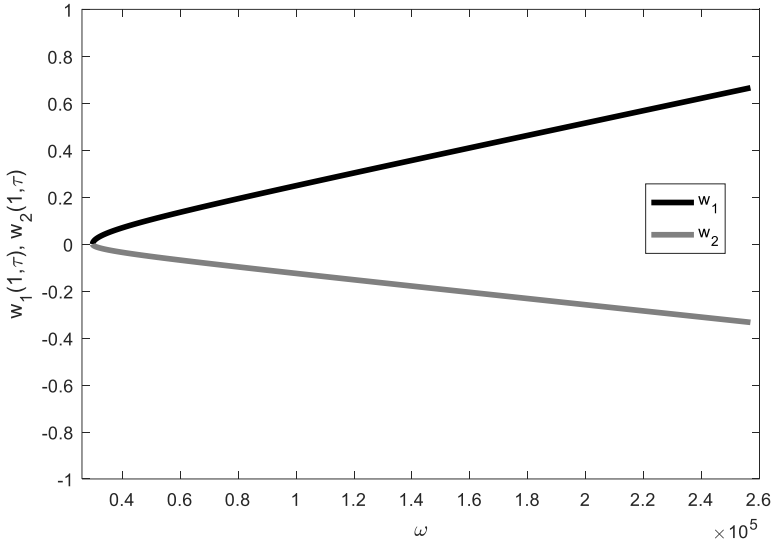

Fig. 4. Free response (R_{eq} = 1) of the noncoaxial vibrational mode of the free end z = 1 of DWCNT.

Fig. 3 establishes the basis for coaxial vibrations, where the geometric concentricity of the CNTs is maintained. In this case the following conclusion can be made $u_1 = u_2$ [14], Eq. (26):

$$e \cdot r_{10} + f \cdot r_{20} - c \cdot r_{10} - d \cdot r_{20} = 0 \tag{38}$$

4.2 COAXIAL PARAMETRIC RESONANCE

For coaxial parametric resonance, the *AC* frequency Ω^* is near coaxial frequency $\bar{\omega}_1$:

$$\Omega^* T_0 = \bar{\omega}_1 T_0 + \sigma T_1 \tag{39}$$

where σ is the detuning parameter for the frequency of actuation. Substituting Eq. (35) with $\omega = \bar{\omega}_1$ into Eq. (34) and rewriting the amplitudes in polar form

$$p = \frac{1}{2} a_1 e^{i\beta}, \; q = \frac{1}{2} a_2 e^{i\beta} \tag{40}$$

yields the following secular terms expression equated to zero:

$$\begin{aligned} &-i\bar{\omega}_1 a_1' - i\bar{\omega}_1 a_1 (i\beta') - \frac{1}{2} i\bar{\omega}_1 e^2 b^* a_1 + \frac{1}{8} \alpha_1 \delta e^2 g_1 \left(2 + e^{2i(\sigma T_1 - \beta)}\right) a_1 + \\ &\frac{1}{16} \alpha_3 \delta e^4 g_3 \left(3 + 2e^{2i(\beta - \sigma T_1)}\right) {a_1}^3 = 0 \end{aligned} \tag{41}$$

Denote

$$\gamma = \sigma T_1 - \beta \tag{42}$$

Applying steady-state assumptions $\gamma' = a_1' = 0$, the imaginary and real components of Eq. (41) yield to zero amplitude steady-state solutions, and non-zero amplitude steady-state solutions given by the following amplitude-frequency a_1, σ equations:

$$a_1 = \sqrt{\frac{8e^2 b^* \bar{\omega}_1}{\alpha_3 \delta e^4 g_3} \cdot \frac{1}{\sin 2\gamma} - \frac{2\alpha_1 g_1}{\alpha_3 e^2 g_3}} \tag{43}$$

$$\sigma = -\frac{\alpha_1 \delta e^2 g_1}{8\bar{\omega}_1} \left(2 + \cos 2\gamma\right) - \frac{\alpha_3 \delta e^4 g_3}{16\bar{\omega}_1} \left[3 + 2\cos 2\gamma\right] {a_1}^2 \tag{44}$$

4.3 COAXIAL PRIMARY RESONANCE

For coaxial primary resonance, the *AC* frequency Ω^* is near-half coaxial frequency $\bar{\omega}_1$:

$$\Omega^* T_0 = \frac{\bar{\omega}_1 T_0}{2} + \sigma T_1 \tag{45}$$

Similar to the coaxial parametric resonance, the following secular terms result:

$$\begin{aligned} &-i\bar{\omega}_1 a_1' - i\bar{\omega}_1 a_1 (i\beta') - \frac{1}{2} i\bar{\omega}_1 e^2 b^* a_1 + \frac{1}{4}\alpha_0 \delta e g_0 e^{i(2\sigma T_1 - \beta)} + \frac{1}{4}\alpha_1 \delta e^2 g_1 a_1 + \\ &\left[\frac{1}{16}\alpha_2 \delta e^3 g_2 e^{i(\beta - 2\sigma T_1)} + \frac{1}{8}\alpha_2 \delta e^3 g_2 e^{i(2\sigma T_1 - \beta)}\right] {a_1}^2 + \frac{3}{16}\alpha_3 \delta e^4 g_3 e^{i(2\sigma T_1 - \beta)} {a_1}^3 = 0 \end{aligned} \tag{46}$$

Substitute Eq. (42) into Eq. (46) and applying steady-state assumptions $\gamma' = a_1' = 0$, the imaginary and real components of Eq. (46) yield to zero amplitude steady-state solutions, and non-zero amplitude steady-state solutions given by the following amplitude-frequency a_1, σ equations:

$$a_1 = \frac{\frac{1}{2} b^* e^2 \bar{\omega}_1 \pm \sqrt{\left(\frac{1}{2} b^* e^2 \bar{\omega}_1\right)^2 - \frac{1}{16}\alpha_0 \alpha_2 \delta^2 e^4 g_0 g_2 \sin^2\gamma}}{\frac{1}{8}\alpha_2 \delta e^3 g_2 \sin\gamma} \tag{47}$$

$$\sigma = -\frac{1}{2\bar{\omega}_1}\left[\frac{1}{4}\alpha_0 \delta e g_0 \frac{\cos\gamma}{a_1} + \frac{1}{4}\alpha_1 \delta e^2 g_1 + \frac{3}{16}\alpha_2 \delta e^3 g_2 \cos\gamma a_1 + \frac{3}{16}\alpha_3 \delta e^4 g_3 {a_1}^2\right] \tag{48}$$

CHAPTER V

REDUCED ORDER MODEL

Reduced Order Models (ROMs) with two or more modes of vibration are used in this thesis. Equation (8) can be written as follows:

$$\begin{cases} A^* \dfrac{\partial^2 w_1}{\partial \tau^2} + I^* \dfrac{\partial^4 w_1}{\partial z^4} = \overline{f}_{vdWT-T} \\ \dfrac{\partial^2 w_2}{\partial \tau^2} + \dfrac{\partial^4 w_2}{\partial z^4} = -b^* \dfrac{\partial w_2}{\partial \tau} - \overline{f}_{vdWT-T} + \dfrac{\delta \cos^2 \Omega^* \tau}{\sum_{k=0}^{5} a_k w_2^k} \end{cases} \tag{49}$$

where f_{elec} was replaced by a fifth-degree Taylor polynomial at the denominator.

5T ROM is more accurate for both weak and strong nonlinearities, as well as for both low and high amplitudes. ROM accuracy increases with the number of modes of vibrations considered. The solutions of the dimensionless deflections are assumed as follow:

$$\begin{cases} w_1(z,\tau) = \sum_{i=1}^{N} u_i(\tau)\phi_i(z) \\ w_2(z,\tau) = \sum_{i=1}^{N} v_i(\tau)\phi_i(z) \end{cases} \tag{50}$$

where N is the number of ROM terms (modes of vibration), u_i and v_i are the time functions to be determined, and ϕ_i are cantilever mode shapes. Note that $\phi_i(1)$ is the value of the mode shape at the tip (free end) of the DWCNT resonator. Substituting Eq. (51) into Eq. (49) and multiplying

the second equation by $\sum_{k=0}^{5} a_k w_2^k$, and then multiply the entire system of equations by the operator $\int_0^1 \bullet \phi_n(z)dz$ yields:

$$A^* \sum_{i=1}^{N} \frac{\partial^2 u_i}{\partial \tau^2} h_{ni} = -I^* \sum_{i=1}^{N} \omega_i^{\,2} u_i h_{ni} + c_1^{\,*} \left(\sum_{i=1}^{N} v_i h_{ni} - \sum_{i=1}^{N} u_i h_{ni} \right) + c_3^{\,*} \left(\sum_{i=1}^{N} v_i h_{ni} - \sum_{i=1}^{N} u_i h_{ni} \right)^3 \tag{51}$$

$$\begin{aligned}
&\sum_{i=1}^{N} \frac{\partial^2 v_i}{\partial \tau^2} \left(a_0 h_{ni} + \sum_{k=1}^{5} a_k \sum_{j_1 \ldots j_{k=1}}^{N} v_{j_1 \ldots} v_{j_k} h_{nij_1 \ldots j_k} \right) = \\
&-b^* \sum_{i=1}^{N} \frac{\partial v_i}{\partial \tau} \left(a_0 h_{ni} + \sum_{k=1}^{5} a_k \sum_{j_1 \ldots j_{k=1}}^{N} v_{j_1 \ldots} v_{j_k} h_{nij_1 \ldots j_k} \right) - \\
&\sum_{i=1}^{N} \omega_i^{\,2} v_i \left(a_0 h_{ni} + \sum_{k=1}^{5} a_k \sum_{j_1 \ldots j_{k=1}}^{N} v_{j_1 \ldots} v_{j_k} h_{nij_1 \ldots j_k} \right) - \\
&c_1^{\,*} \left[\sum_{i=1}^{N} (v_i - u_i) \left(a_0 h_{ni} + \sum_{k=1}^{5} a_k \sum_{j_1 \ldots j_{k=1}}^{N} v_{j_1 \ldots} v_{j_k} h_{nij_1 \ldots j_k} \right) \right] - \\
&c_3^{\,*} \left[\sum_{i=1}^{N} (v_i - u_i)^3 \left(a_0 h_{ni} + \sum_{k=1}^{5} a_k \sum_{j_1 \ldots j_{k=1}}^{N} v_{j_1 \ldots} v_{j_k} h_{nij_1 \ldots j_k} \right) \right] + \delta h_n \cos^2 \Omega^* \tau
\end{aligned} \tag{52}$$

where $n = 1, 2, \ldots, N$, and $i, j_1 \ldots j_k = 1, 2, \ldots, N$. The values of a_k coefficients are given in Table 8, and coefficients h are as follows:

$$h_n = \int_0^1 \phi_n dz, h_{ni} = \int_0^1 \phi_i \phi_n dz, h_{nij_1} = \int_0^1 \phi_i \phi_{j_1} \phi_n dz \cdots h_{nij_1 \ldots j_k} = \int_0^1 \phi_i \phi_{j_1} \ldots \phi_{j_k} \phi_n dz \tag{53}$$

Table 8. Coefficients of Electrostatic Denominator $\sum_{k=0}^{5} a_k w_2^k$

Symbol	*Value*
a_0	24.61700
a_1	-34.54542
a_2	5.96045
a_3	1.65281
a_4	0.74268
a_5	0.41202

One should notice that $h_{ni} = \delta_{ni}$ where δ_{ni} is Kronecker's delta. For an N-Term ROM, Eq. (20) may be re-written as follows:

$$\begin{bmatrix} A^* & \cdots & 0 & 0 & \cdots & 0 \\ \vdots & \ddots & \vdots & \vdots & \ddots & \vdots \\ 0 & \cdots & A^* & 0 & \cdots & 0 \\ 0 & \cdots & 0 & 1 & \cdots & 0 \\ \vdots & \ddots & \vdots & \vdots & \ddots & \vdots \\ 0 & \cdots & 0 & 0 & \cdots & 1 \end{bmatrix} \begin{bmatrix} \ddot{u}_1 \\ \vdots \\ \ddot{u}_N \\ \ddot{v}_1 \\ \vdots \\ \ddot{v}_N \end{bmatrix} + \begin{bmatrix} C_1^* + I^* \omega_{1I}^2 & \cdots & 0 & -c_1^* & \cdots & 0 \\ \vdots & \ddots & \vdots & \vdots & \ddots & \vdots \\ 0 & \cdots & C_1^* + I^* \omega_{NI}^2 & 0 & \cdots & -c_1^* \\ -c_1^* & \cdots & 0 & C_1^* + \omega_{1O}^2 & \cdots & 0 \\ \vdots & \ddots & \vdots & \vdots & \ddots & \vdots \\ 0 & \cdots & -c_1^* & 0 & \cdots & C_1^* + \omega_{NO}^2 \end{bmatrix} \begin{bmatrix} u_1 \\ \vdots \\ v_N \\ u_1 \\ \vdots \\ v_N \end{bmatrix} = \begin{bmatrix} 0 \\ \vdots \\ 0 \\ 0 \\ \vdots \\ 0 \end{bmatrix} \tag{54}$$

Following the same modal analysis procedure outlined in Eqs. (21)-(25), the modal coordinate transformation for an N-Term ROM becomes:

$$\begin{bmatrix} u_1 \\ \vdots \\ u_N \\ v_1 \\ \vdots \\ v_N \end{bmatrix} = \begin{bmatrix} c_1 & \cdots & 0 & d_1 & \cdots & 0 \\ \vdots & \ddots & \vdots & 0 & \ddots & \vdots \\ 0 & \cdots & c_N & 0 & \cdots & d_N \\ e_1 & \cdots & 0 & f_1 & \cdots & 0 \\ \vdots & \ddots & \vdots & \vdots & \ddots & \vdots \\ 0 & \cdots & e_N & 0 & \cdots & f_N \end{bmatrix} \begin{bmatrix} r_{11} \\ \vdots \\ r_{1N} \\ r_{21} \\ \vdots \\ r_{2N} \end{bmatrix} \tag{55}$$

Subsequently, substituting Eq. (55) into Eq. (50), a ROM is constructed in the modal *r*-coordinate system as:

$$\begin{cases} w_1(z,\tau) = \sum_{i=1}^{N} (c_i r_{1i} + d_i r_{2i})(\tau)\phi_i(z) \\ w_2(z,\tau) = \sum_{i=1}^{N} (e_i r_{1i} + f_i r_{2i})(\tau)\phi_i(z) \end{cases} \tag{56}$$

From Eq. (27) and E. (38), the Modal ROM equations in the *r*-coordinate system are given by:

$$\begin{cases} \sum_{i=1}^{N} \ddot{r}_{1i}\phi_i(z) + b^* \sum_{i=1}^{N} {e_i}^2 \dot{r}_{1i}\phi_i(z) + b^* \sum_{i=1}^{N} e_i f_i \dot{r}_{2i}\phi_i(z) + \sum_{i=1}^{N} {\bar{\omega}_{1i}}^2 r_{1i}\phi_i(z) = \\ \qquad \sum_{i=1}^{N} \dfrac{e_i \delta {V_t}^2}{\sum_{k=0}^{5} a_k \left[(e_i r_{1i} + f_i r_{2i})\phi_i(z) \right]^k} \\ \sum_{i=1}^{N} \ddot{r}_{2i}\phi_i(z) + b^* \sum_{i=1}^{N} e_i f_i \dot{r}_{1i}\phi_i(z) + b^* \sum_{i=1}^{N} {f_i}^2 \dot{r}_{2i}\phi_i(z) + \sum_{i=1}^{N} {\bar{\omega}_{2i}}^2 r_{2i}\phi_i(z) = \\ \qquad \sum_{i=1}^{N} \dfrac{e_i \delta {V_t}^2}{\sum_{k=0}^{5} a_k \left[(e_i r_{1i} + f_i r_{2i})\phi_i(z) \right]^k} \end{cases} \tag{57}$$

Equations (57) are multiplied by the denominators of their right-hand sides. Then the resulting equations are multiplied by $\phi_n(z)$ and integrated from 0 to 1, $n = 1,2,\ldots,N$. After the system is numerically integrated, Eq. (56) is deconstructed such that $w_1 = w_{11N} + w_{12N}$ and $w_2 = w_{21N} + w_{22N}$ as defined below:

$$w_{11N}(z,\tau)=\sum_{i=1}^{N} c_i \cdot r_{1i}(\tau)\phi_i(z) \quad , \quad w_{12N}(z,\tau)=\sum_{i=1}^{N} d_i \cdot r_{2i}(\tau)\phi_i(z)$$
$$w_{21N}(z,\tau)=\sum_{i=1}^{N} e_i \cdot r_{1i}(\tau)\phi_i(z) \quad , \quad w_{22N}(z,\tau)=\sum_{i=1}^{N} f_i \cdot r_{2i}(\tau)\phi_i(z) \tag{58}$$

For instance $w_{12N}(z,\tau)$ is the noncoaxial modal deflection of w_1 of inner CNT containing the $r_{2i}(\tau)$ noncoaxial modal coordinates, for *N* terms ROM. The reason for this decomposition is the later use of modal truncation method [14] for *N* = 5,6, i.e. 5T-ROM and 6T-ROM. In this method, modes of frequency far from excitation frequency can be neglected. Truncated models reduce the size of the ROM, and therefore allow for numerical simulations of ROMs with larger number *N* of modes, such as 5T-ROM and 6T-ROM. In this work, the terms w_{12N} and w_{22N} containing the noncoaxial modal coordinates $r_{2i}(\tau)$, in the tested cases are shown to be negligible, and therefore to not contradict the truncation method. The system of Eqs. (57) is replaced by the truncated model

$$\sum_{i=1}^{N} \ddot{r}_{1i}\phi_i(z)+b^*\sum_{i=1}^{N} {e_i}^2\dot{r}_{1i}\phi_i(z)+\sum_{i=1}^{N} {\bar{\omega}_{1i}}^2 r_{1i}\phi_i(z)=\sum_{i=1}^{N}\frac{e_i\delta {V_t}^2}{\sum_{k=0}^{5} a_k\left[e_i r_{1i}\phi_i(z)\right]^k} \tag{59}$$

Similar to Eqs. (51) - (52), Eq. (59) is multiplied by the denominators at the right-hand side. Then, the resulting equation is multiplied by $\phi_n(z)$ and integrated from 0 to 1, $n = 1,2,\ldots,N$, resulting into a system of *N* second order differential equations

$$\begin{aligned}
&\sum_{i=1}^{N}\frac{\partial^2 r_{1i}}{\partial\tau^2}\left(\sum_{j_1=1}^{N} a_0 h_{nj_1}+\sum_{k=1}^{5} a_k \sum_{j_2\ldots j_{k=1}}^{N} e_{j_2\ldots}e_{j_k} r_{1j_2\ldots}r_{1j_k} h_{nj_1 j_2\ldots j_k}\right)= \\
&-b^*\sum_{i=1}^{N} {e_i}^2\frac{\partial v_i}{\partial\tau}\left(\sum_{j_1=1}^{N} a_0 h_{nj_1}+\sum_{k=1}^{5} a_k \sum_{j_2\ldots j_{k=1}}^{N} e_{j_2\ldots}e_{j_k} r_{1j_2\ldots}r_{1j_k} h_{nj_1 j_2\ldots j_k}\right)- \\
&\sum_{i=1}^{N} {\bar{\omega}_{1i}}^2 v_i\left(\sum_{j_1=1}^{N} a_0 h_{nj_1}+\sum_{k=1}^{5} a_k \sum_{j_2\ldots j_{k=1}}^{N} e_{j_2\ldots}e_{j_k} r_{1j_2\ldots}r_{1j_k} h_{nj_1 j_2\ldots j_k}\right)+\sum_{i=1}^{N} e_i\delta h_n\cos^2\Omega^*\tau
\end{aligned} \tag{60}$$

CHAPTER VI

NUMERICAL SIMULATIONS

AUTO-07P, a software package for continuation and bifurcation, is utilized to calculate ROM solutions and predict the frequency-amplitude response. MATLAB software is used to simulate the frequency-amplitude response predicted by MMS. Matlab is also used to numerically integrate ROMs and predict time responses of the structure. In this work, time responses for specified parameters are obtained using a MATLAB ODE solver, namely *ode15s*. One should mention that *ode15s* is a "multistep, variable order solver based on numerical differentiation formulas" [30-31].

MMS is a perturbation technique [32-34] that is utilized due to the ease of identifying amplitude-frequency responses for weak nonlinearities and low amplitudes. MMS provides an approximate analytical solution for ROM with one mode of vibration. To investigate solutions of higher amplitude and verify those of smaller amplitude, ROMs with a larger number of modes of vibration is used. While more accurate at higher amplitudes, these ROMs are more time-consuming.

6.1 PARAMETRIC RESONANCE – FREQUENCY RESPONSE (COAXIAL)

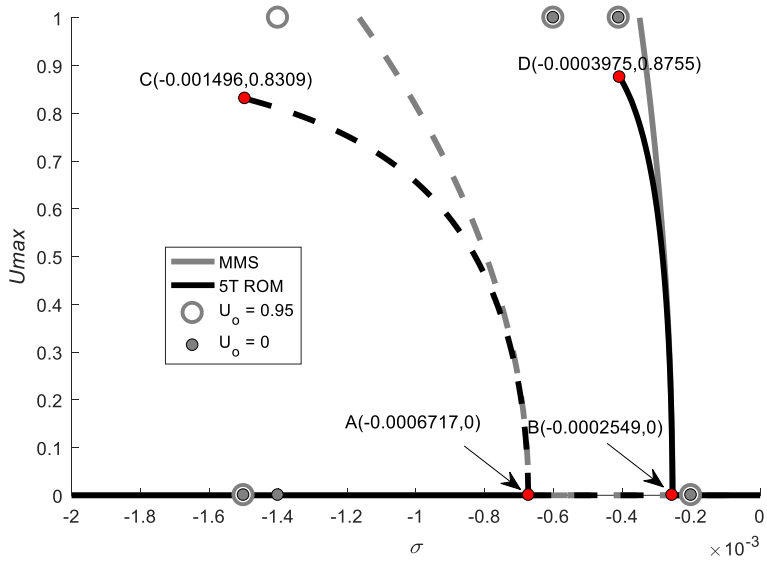

Fig. 5. Amplitude-frequency response, parametric resonance, using five terms (5T) ROM (present work) and MMS, $b^* = 0.0003$, $\delta = 0.15$.

Fig. 5 shows the amplitude-frequency response of the DWCNT under parametric resonance using 5T ROM and a direct comparison with MMS. Dash and solid lines represent the unstable and stable solutions, respectively. This response is characterized by two Hopf bifurcations: subcritical with the bifurcation point at *A* and the supercritical with the bifurcation point at *B*. For 5T ROM, the unstable branch (left) of the subcritical bifurcation divides the area into two distinct regions. For initial amplitudes below the dash line, the system settles to zero amplitudes, while for initial amplitudes above the dash line the resonator is "pulled-in" to the ground plate or settles to large amplitudes. For frequencies below that of point C, the MEMS resonator settles to zero amplitude regardless of initial amplitude. For frequencies between those of point A and D, the resonator is pulled-in regardless of initial amplitude (contact of the MEMS cantilever with the ground plate, which corresponds to a dimensionless amplitude of 1, i.e. dimensional amplitude equals the gap). One can observe that for amplitudes less than 0.4 of the gap, the ROM and MMS are in excellent agreement. For amplitudes larger than 0.4 of the gap,

MMS cannot predict the behavior of the system, a limitation of this method. It underestimates the softening effect and does not predict the pull-in phenomenon from large amplitudes, points C and D.

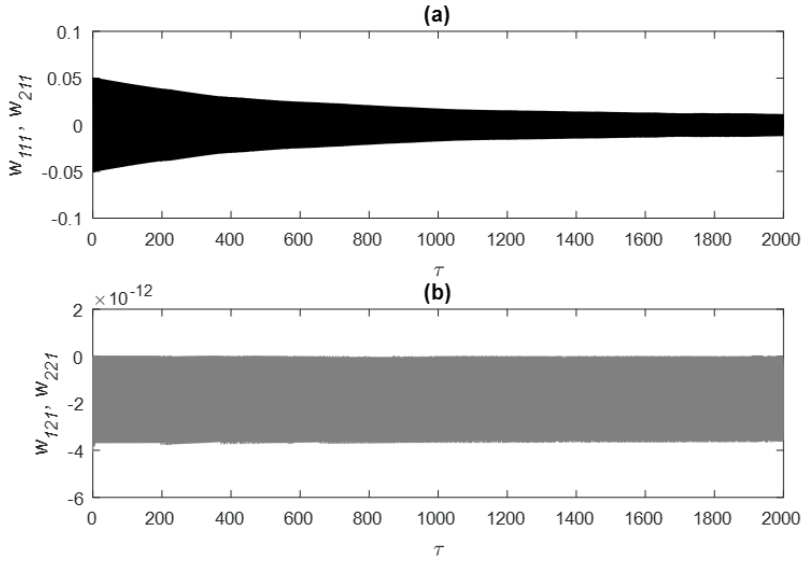

Fig. 6. Time response using 1T ROM for DWCNT resonator for AC frequency near natural frequency. Initial amplitude U_0 = 0.05, b^* = 0.0003, δ = 0.15, σ = 0. (a) r_{1i} only (b) r_{2i} only.

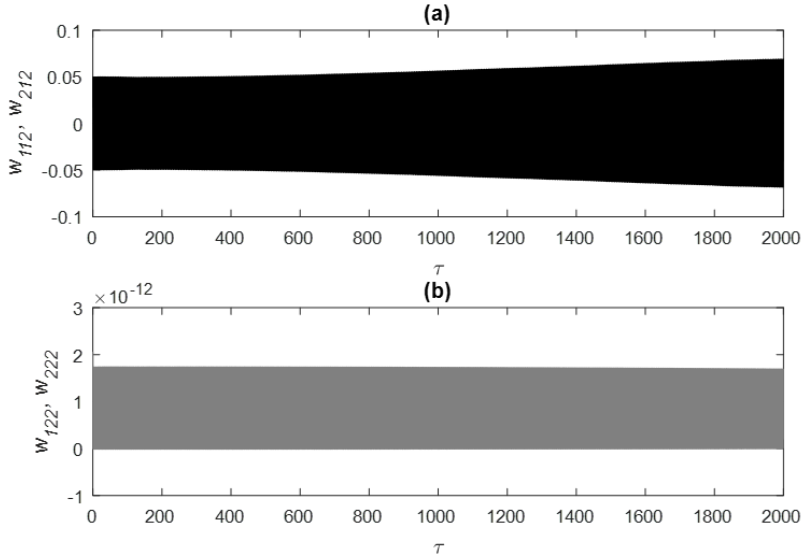

Fig. 7. Time response using 2T ROM for DWCNT resonator for AC frequency near natural frequency. Initial amplitude U_0 = 0.05, b^* = 0.0003, δ = 0.15, σ = 0. (a) r_{1i} only (b) r_{2i} only.

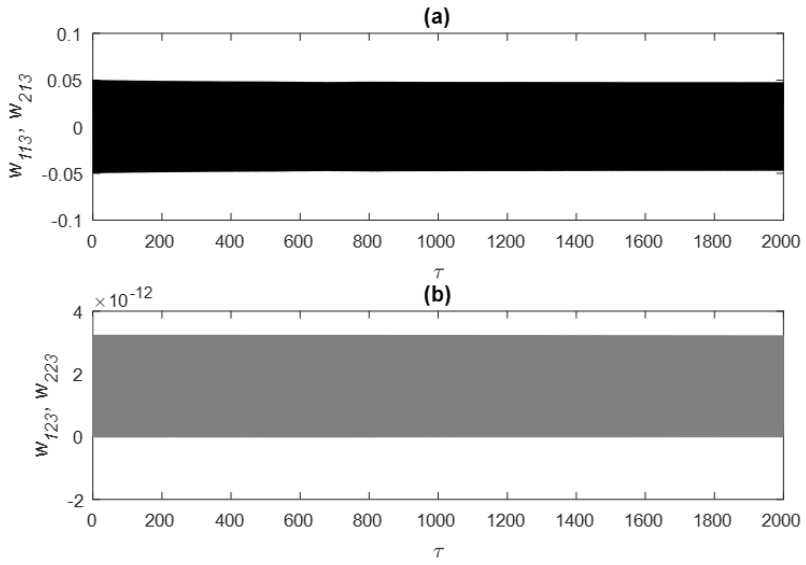

Fig. 8. Time response using 3T ROM for DWCNT resonator for AC frequency near natural frequency. Initial amplitude U_0 = 0.05, b^* = 0.0003, δ = 0.15, σ = 0. (a) r_{1i} only (b) r_{2i} only.

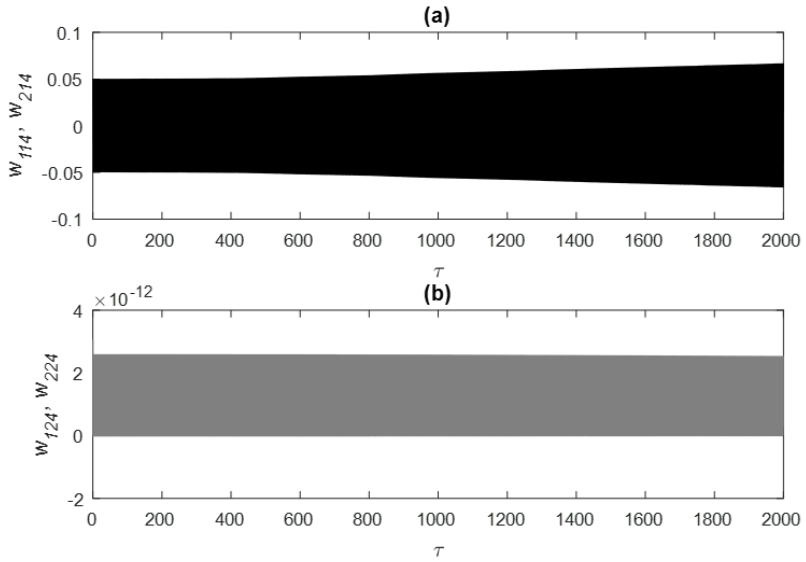

Fig. 9. Time response using 4T ROM for DWCNT resonator for AC frequency near natural frequency. Initial amplitude U_0 = 0.05, b^* = 0.0003, δ = 0.15, σ = 0. (a) r_{1i} only (b) r_{2i} only.

In Figs. 6-9, time responses for b^* = 0.0003, δ = 0.15, small initial amplitude, U_0 = 0.05, and zero detuning frequency have been simulated for 1T ROM, 2T ROM, 3T ROM, and 4T ROM, respectively. The utility of expanding the ROM in the modal coordinate system is that this

allows for one to see what occurs in the coaxial and noncoaxial resonances. The modal amplitudes represented in Figs. 6-9 are the decomposition of Eq. (52) as shown in Eq. (54) that relate the modal coordinates to the dimensionless deflections. A small initial amplitude of U_0 = 0.05 was chosen to compare different number of terms in the ROM since the differences are only to be expected in higher amplitudes. This intentional approach of setting each N-term ROM to small initial amplitudes allows for a more direct comparison of the systematic influences of modal amplitudes devoid of any amplitude difference related to number of terms. Note that any numerical inaccuracies/discrepancies in Fig. 6 (1T ROM) are likely due to the lack of robustness from a one-term ROM expansion. Nevertheless, the same orders of magnitude as shown in Figs. 7-9 are observed. It is important to note that the resonant case investigated in this thesis is both *far* from the noncoaxial resonance and thus devoid of any internal resonance. From perturbation methods, such as MMS, the non-resonant mode is "damped out" after steady-state assumptions are made [18]. The importance of these results is that they present a numerical investigation (ROM) of both resonant (coaxial) and non-resonant (noncoaxial) with no steady-state assumptions that are typically made in perturbation methods. The numerical cases investigated in Figs. 6-9 confirm that the $r_{2i}(\tau)$ modal amplitudes, which form the modal superposition of w_{12N} and w_{22N}, have no influence in the deflections outlined in Eq. (52). Therefore, since the *AC* actuation frequency is near the first natural frequency of the coaxial vibration, the tip deflection of the DWCNT resonator may be defined satisfactorily by considering only $r_{1i}(\tau)$, since $r_{2i}(\tau)$ values are in the 10^{-12} order of magnitude. The concept of modal system reduction is also known as modal truncation, with the general basis that "certain modes occur at frequencies well outside the system's domain of operating frequencies…these modes can be safely removed from the model with minimal approximation error since they [do] not contribute much to the relevant

dynamics of the system" [35]. It is important to note that the full-order modal responses were numerically compared with time responses and bifurcation diagrams up to 4T ROM with their modally truncated (no r_2) counterparts. The errors were observed in the 10^{-12} range, thus, for higher order ROM, the expansions are performed using only $r_{1i}(\tau)$, which not only reduces the system of equations by half, but also reduces computational time in the MATLAB time responses.

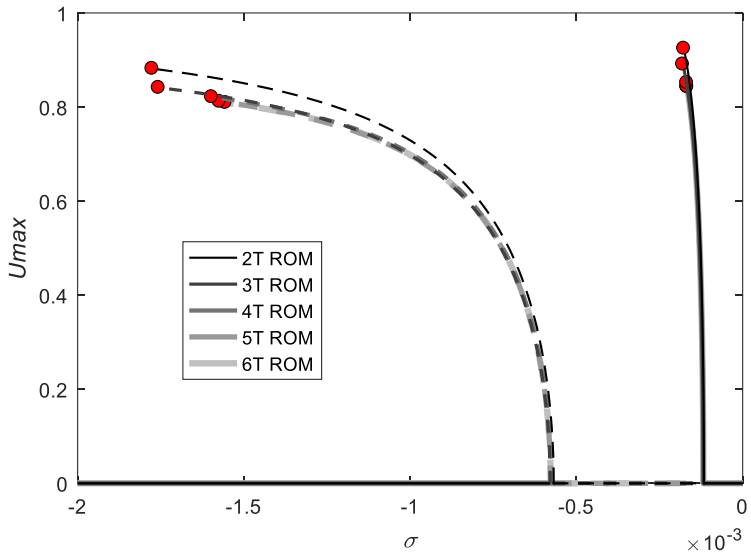

Fig. 10. ROM AUTO convergence of the amplitude-frequency response for DWCNT resonator using two terms (2T ROM), three terms (3T ROM), …, and six terms (6T ROM). AC frequency near natural frequency. $b^* = 0.0001$, $\delta = 0.15$.

Fig. 10 illustrates the convergence of the ROM method. Using numerical simulation with AUTO-07P, the number of terms considered is between two and six. One can see that the difference between 5T ROM AUTO and 6T ROM AUTO is in the 10^{-3} order of magnitude, meaning that tip deflections can be achieved with adequate accuracy by 5T ROM with reduced computational time. Between the two bifurcation points, the zero amplitude steady-states are unstable, and the system experiences either pull-in or settles to nonzero steady-state amplitudes on the stable branch, regardless of the initial amplitude.

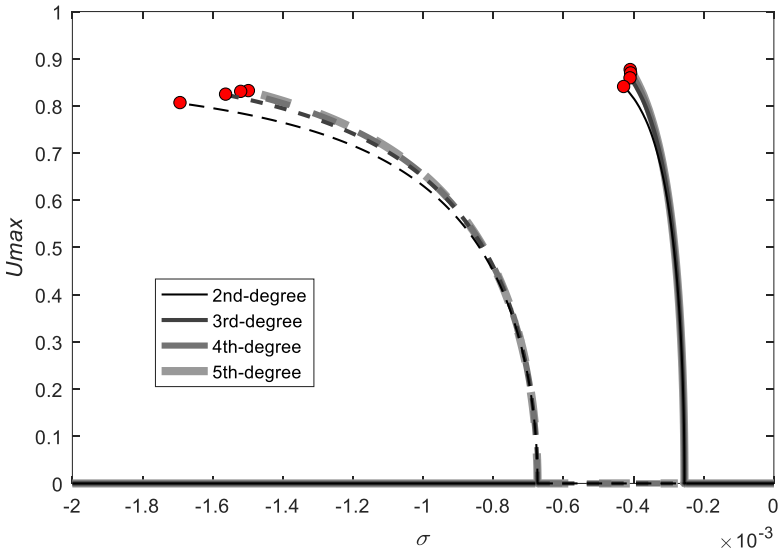

Fig. 11. ROM AUTO Taylor denominator convergence of the amplitude-frequency response for DWCNT resonator using five terms (5T ROM). AC frequency near natural frequency. b^* =0.0003, δ = 0.15.

Fig. 11 shows the solution convergence to increasing the degree of the Taylor polynomial in the denominator for ROM. Similar to the term convergence shown in Fig. 10, a numerical solution convergence may be seen in the fifth degree of the electrostatic force (polynomial) in the denominator.

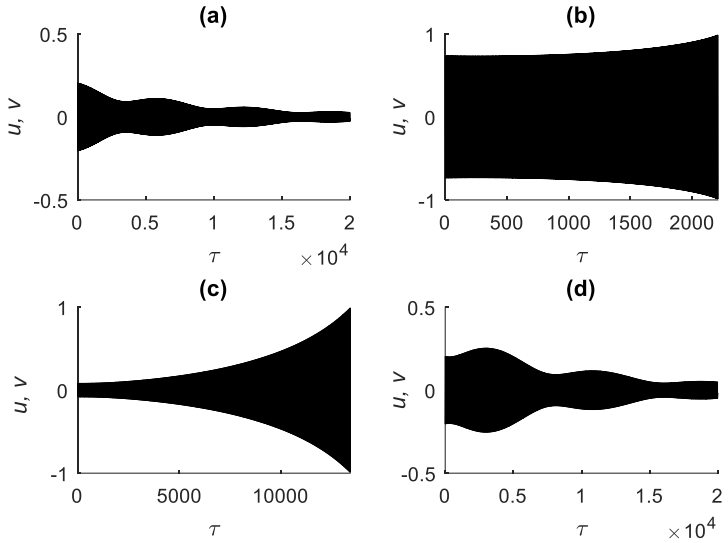

Fig. 12. Time response using 5T ROM for DWCNT resonator for AC frequency near natural frequency; b^* = 0.0003, δ = 0.15, (a) Initial amplitude U_0 = 0.25, σ = -0.001, (b) Initial amplitude U_0 = 0.9, σ = -0.001, (c) Initial amplitude U_0 = 0.1, σ = -0.0004, (d) Initial amplitude U_0 = 0.25, σ = 0.

Figs. 12 (a)-(d) show time responses using 5T ROM for b^* = 0.0003 and δ = 0.15 considering various initial amplitudes and values of detuning frequency, where $u = w_1(1,\tau)$ and $v = w_2(1,\tau)$. They are in excellent agreement with the frequency responses from 5T ROM AUTO and MMS, as shown in Fig. 5. Pull-in phenomena is evidenced in Fig. 12 (b) and Fig. 12 (c), while attenuation to a zero-amplitude results can be seen in Fig. 12 (a) and Fig. 12 (d). The observed beating behavior is typical in the transient response nonlinear oscillators subjected to harmonic forcing [36-37]. It is important to note that a large enough time span is chosen for each case in order for the responses to reach a steady-state solution.

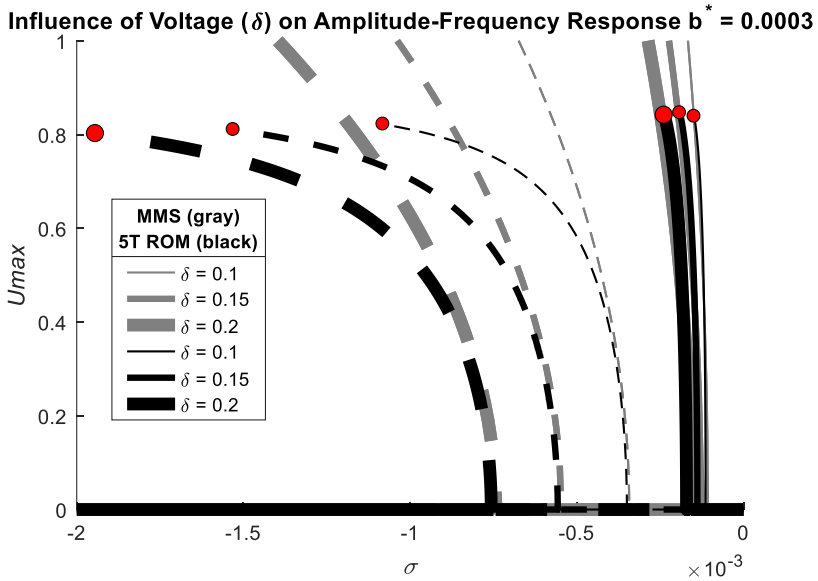

Fig. 13. Effect of applied voltage, δ, on frequency response, MMS and ROM AUTO.

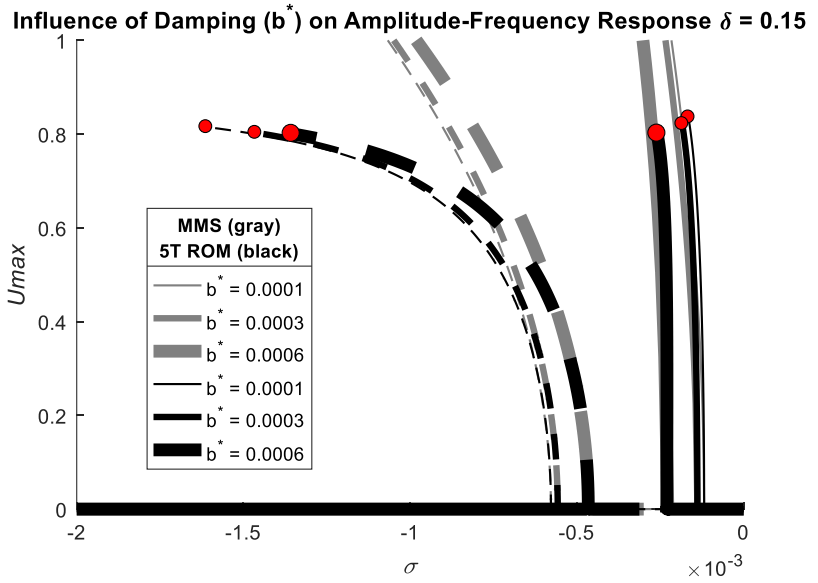

Fig. 14. Effect of dimensionless damping, *b**, on frequency response, MMS and ROM AUTO.

Fig. 13 shows the effect of applied voltage on the amplitude-frequency response. The voltage parameter δ has a significant effect on the response. Increasing the voltage parameter, increases the distance between the Hopf bifurcations, therefore the range of frequencies for which the system experiences pull-in is significantly larger. Also, both branches shift to lower frequencies, the unstable branch more than the stable branch. Furthermore, increasing the voltage parameter shows an increase in softening effect.

Fig. 14 illustrates the effect of dimensionless damping on the amplitude-frequency response. As damping increases, the distance between the subcritical and supercritical Hopf bifurcations decreases, until the unstable and stable branches coalesce for high enough damping coefficients. Increasing damping reduces the range of frequencies for which the DWCNT undergoes large amplitudes or pull-in.

6.2 PARAMETRIC RESONANCE – VOLTAGE RESPONSE (COAXIAL)

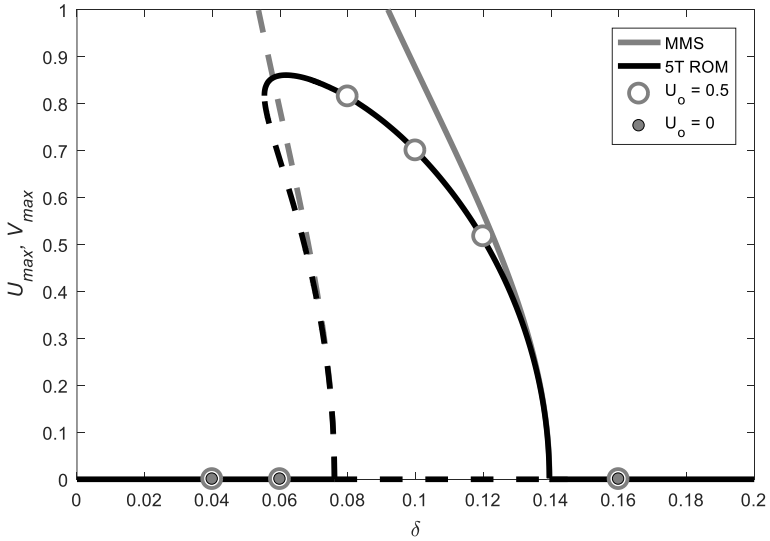

Fig. 15. Amplitude-voltage response, parametric resonance, using five terms (5T) ROM and MMS, b^* = 0.00035, σ = -0.00025

Fig. 15 shows the amplitude-voltage response of the DWCNT under parametric resonance using 5T ROM and a direct comparison with MMS. Dash and solid lines represent the unstable and stable solutions, respectively. This response is characterized by two Hopf bifurcations at zero amplitude: subcritical with the bifurcation point at the left (stable to unstable) and the supercritical with the bifurcation point at the right (unstable to stable). From 5T ROM time responses, it is clear that for any initial amplitude to the left of the subcritical Hopf birfurcation and to the right of the supercritical Hopf bifurcation, the deflection will attenuate to zero amplitude. Conversely, for initial amplitudes greater than zero between the Hopf bifurcation points, the deflection will tend toward the higher amplitude, stable branch. One can observe that for amplitudes less than 0.4 of the gap, the ROM and MMS are in excellent agreement. For amplitudes larger than 0.4 of the gap, MMS cannot predict the behavior of the system, a limitation of this method. It underestimates the softening effect and fails to predict the saddle-node bifurcation that occurs at higher amplitudes.

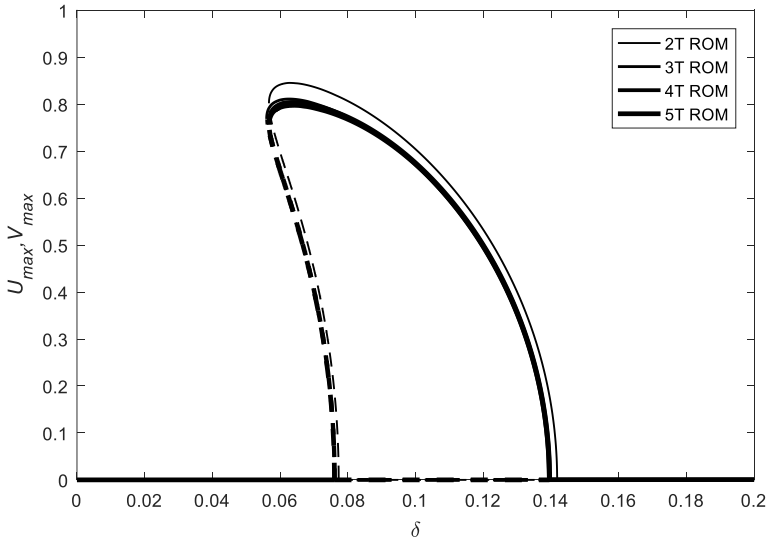

Fig. 16. ROM AUTO convergence of the amplitude-voltage response for DWCNT resonator using two terms (2T ROM), three terms (3T ROM), …, and five terms (5T ROM). AC frequency near natural frequency. b^* = 0.00035, σ = -0.00025

Fig. 16 illustrates the convergence of the ROM method. Using numerical simulation with AUTO-07P, the number of terms considered is between two and five. One can see that the difference between 4T ROM AUTO and 5T ROM AUTO is only at higher amplitudes. The 2T ROM AUTO solutions has a shift in the bifurcation points, indicative of low accuracy when not enough terms are considered. For this case, there is no need to check for higher terms above 5T ROM since five terms is shown to be appropriate for solutions.

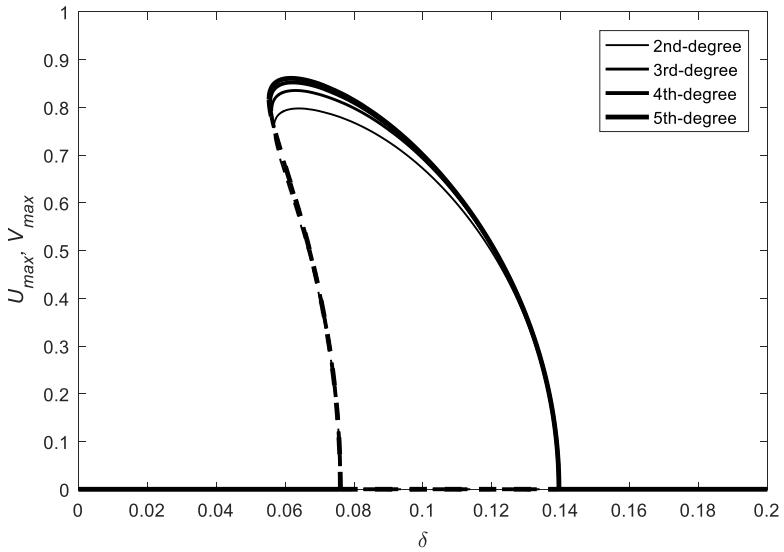

Fig. 17. ROM AUTO Taylor denominator convergence of the amplitude-voltage response for DWCNT resonator using five terms (5T ROM). AC frequency near natural frequency. b^* = 0.00035, σ = -0.00025

Fig. 17 shows the solution convergence to increasing the degree of the Taylor polynomial in the denominator for 5T ROM. Similar to the term convergence shown in Fig. 16, a numerical solution convergence may be seen in the fifth degree of the electrostatic force (polynomial) in the denominator, with an excellent approximation of higher amplitudes.

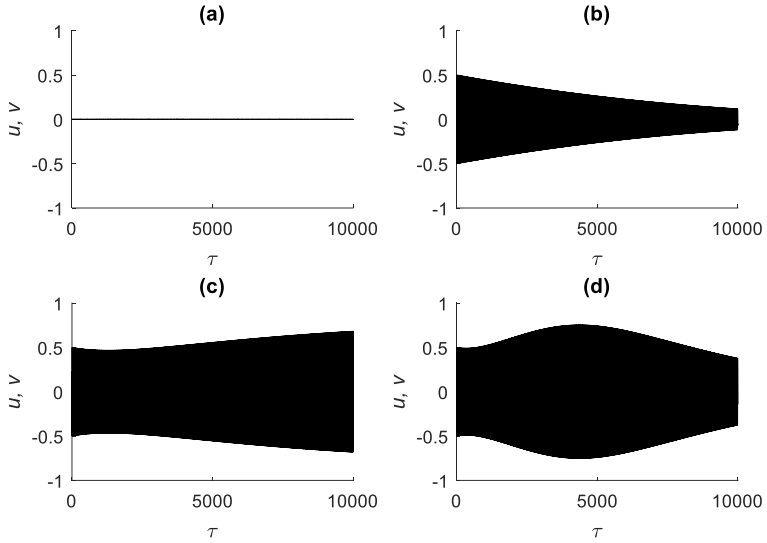

Fig. 18. Time response using 5T ROM for DWCNT resonator for AC frequency near natural frequency; b^* = 0.00035, σ = -0.00025, (a) Initial amplitude U_0 = 0, δ = 0.04, (b) Initial amplitude U_0 = 0.5, δ = 0.04, (c) Initial amplitude U_0 = 0.5, δ = 0.1, (d) Initial amplitude U_0 = 0.5, δ = 0.16

Figs. 18 (a)-(d) show time responses using 5T ROM for b^* = 0.00035 and σ = -0.00025 considering various initial amplitudes and values of voltage, where $u = w_1(1,\tau)$ and $v = w_2(1,\tau)$. They are in excellent agreement with the frequency responses from 5T ROM AUTO and MMS, as shown in Fig. 15. Fig. 18 (a) and Fig. 18 (b) characterize the behavior to the left of the subcritical Hopf bifurcation, where regardless of initial amplitude, the deflection will settle to the zero amplitude stable solution. Similarly, Fig. 18 (d) shows the behavior to the right of the supercritical Hopf bifurcation, where regardless of initial amplitude, the deflections will reach zero amplitude. Fig. 18 (c) shows the typical behavior of deflections in between the two Hopf bifurcation points, where the solutions will settle at the higher amplitude stable branch.

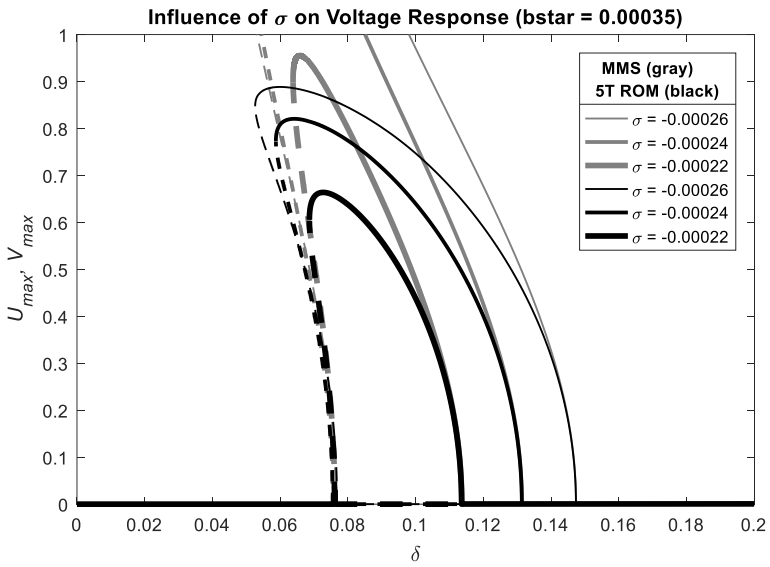

Fig. 19. Effect of detuning frequency, σ, on voltage response, MMS and ROM AUTO

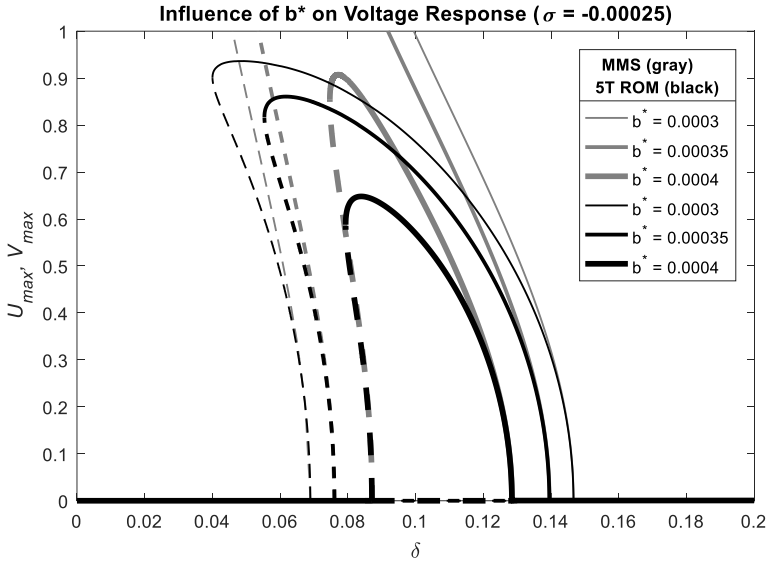

Fig. 20. Effect of dimensionless damping, *b**, on voltage response, MMS and ROM AUTO

Fig. 19 shows the effect of detuning frequency σ on the amplitude-voltage response. Increasing the detuning frequency, i.e, increasing positively, causes both Hopf bifurcation voltages to shift to lower voltages, with a greater shift on the supercritical bifurcation. This is typified by a hardening of the nonlinearity, where the saddle-node bifurcation is shifted to lower amplitudes and higher voltage. Furthermore, the voltage interval between the Hopf bifurcation points for nonzero steady-state amplitudes decreases for increasing values of detuning frequency.

Fig. 20 illustrates the effect of damping b^* on the amplitude-voltage response. Increasing the damping on the electrostatically actuated DWCNT shifts the Hopf subcritical bifurcation voltages to higher voltages and the Hopf supercritical bifurcation voltages to lower voltages. Essentially, increasing values of damping reduces the voltage interval of nonzero steady-state amplitudes, while also reducing the nonlinear behavior and peak amplitude.

6.3 PRIMARY RESONANCE – FREQUENCY RESPONSE (COAXIAL)

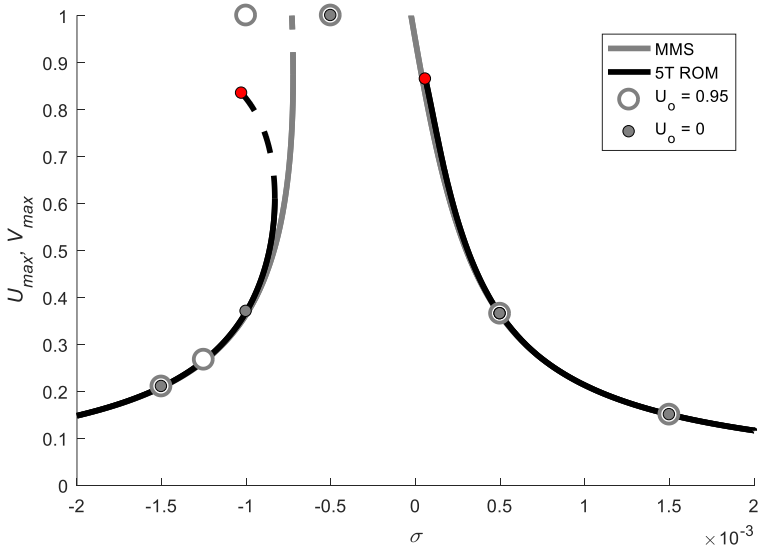

Fig. 21. Amplitude-frequency response, primary resonance, using five terms (5T) ROM and MMS, $b^* = 0.001$, $\delta = 0.15$

Fig. 21 shows the amplitude-frequency response of the electrostatically actuated DWCNT in the case of soft AC of frequency near-half fundamental natural frequency using two methods, namely MMS and ROM. In the ROM method five terms (five modes of vibration) are used. There are three branches (stable-unstable-stable) of the response. The solid branches are stable branches. The dashed branch is unstable. There are two situations to be discussed, first when the system reached steady-state and the frequency is swept up and down, and second when the frequency and initial amplitude (other than steady-state) are given and the frequency is kept constant. In the first situation, as the frequency is swept up from the left, the steady-state amplitude increases along the first solid branch until it reaches the saddle-node bifurcation. At this point the plate loses stability and the amplitude suddenly jumps to a value of 1 (the amplitude reaches the value of the gap), i.e. a pull-in phenomenon occurs (contact between the DWCNT and the ground plate). As the frequency is swept down from larger frequencies the amplitude increases along the unstable branch until the system loses stability and undergoes a pull-in phenomenon. In the second situation, when the frequency is kept constant, the behavior of the system depends on its AC frequency and its initial amplitude. If the frequency is less than the frequency of the endpoint of the unstable branch, then regardless of initial amplitude the plate settles to an amplitude on the left solid branch. If the frequency is between the frequencies of the saddle-node bifurcation and the unstable endpoint, then the behavior of the system depends on the initial amplitude. Therefore for any initial amplitude below the unstable branch, the DWCNT settles to a steady-state amplitude on the left solid branch.

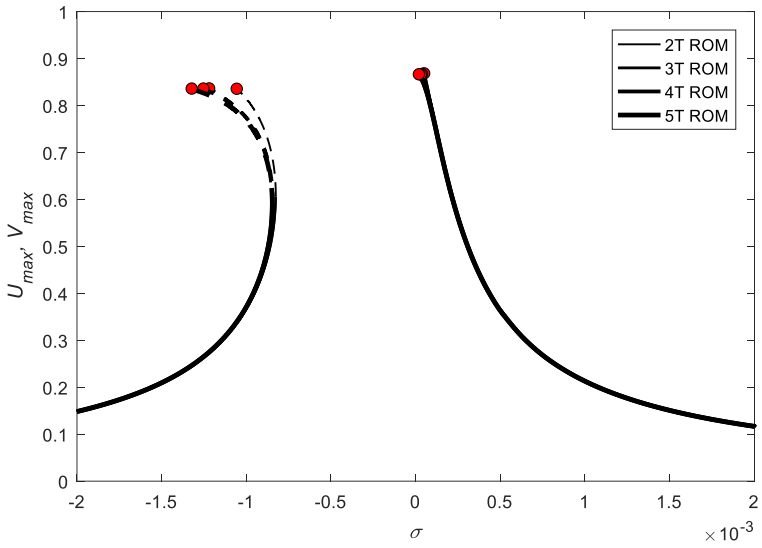

Fig. 22. ROM AUTO convergence of the amplitude-frequency response for DWCNT resonator using two terms (2T ROM), three terms (3T ROM), …, and five terms (5T ROM). AC frequency near-half natural frequency. $b^* = 0.001$, $\delta = 0.15$

Fig. 22 illustrates the convergence of the ROM method. Using numerical simulation with AUTO-07P, the number of terms considered is between two and five. One can see that the difference between the terms is only at higher amplitudes. The convergence of solutions is apparent on the unstable branch, which shifts to lower frequencies. For this case, there is no need to check for higher terms above 5T ROM since five terms is shown to be appropriate for solutions.

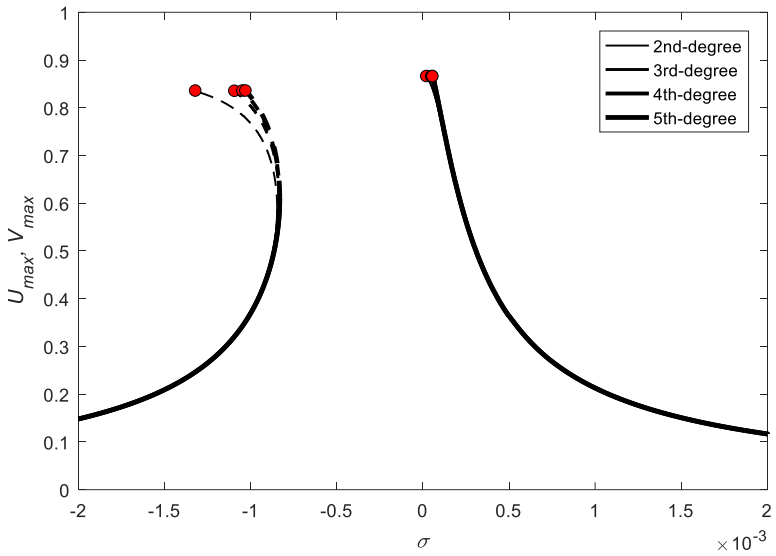

Fig. 23. ROM AUTO Taylor denominator convergence of the amplitude-frequency response for DWCNT resonator using five terms (5T ROM). AC frequency near-half natural frequency. b*=0.001, δ = 0.15

Fig. 23 shows the solution convergence to increasing the degree of the Taylor polynomial in the denominator for 5T ROM. Similar to the term convergence shown in Fig. 22, a numerical solution convergence may be seen in the fifth degree of the electrostatic force (polynomial) in the denominator, with an excellent approximation of higher amplitudes. One can observe the increasing the Taylor polynomial terms shifts the unstable branch to higher amplitudes.

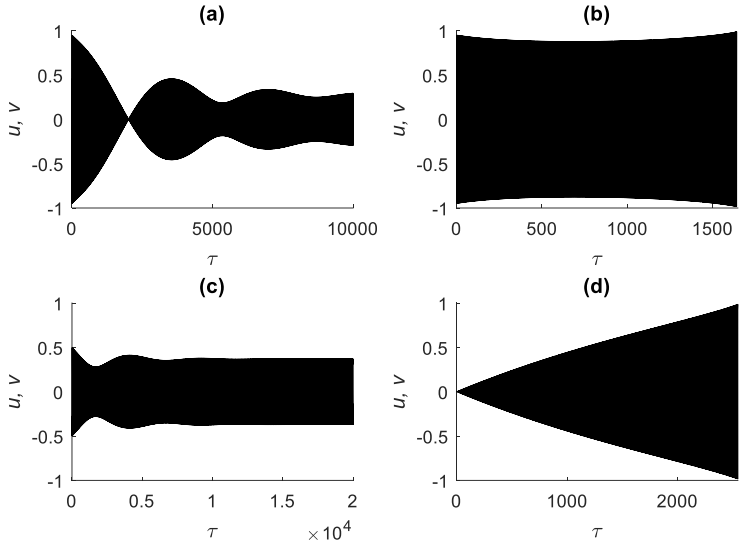

Fig. 24. Time response using 5T ROM for DWCNT resonator for AC frequency near-half natural frequency; $b^* = 0.001$, $\delta = 0.15$, (a) Initial amplitude $U_0 = 0.95$, σ = -0.00125, (b) Initial amplitude $U_0 = 0.95$, σ = -0.001, (c) Initial amplitude $U_0 = 0.5$, σ = -0.001, (d) Initial amplitude $U_0 = 0$, σ = -0.0005

Figs. 24 (a)-(d) show time responses using 5T ROM for $b^* = 0.001$ and $\delta = 0.15$ considering various initial amplitudes and values of detuning frequency, where $u = w_1(1,\tau)$ and $v = w_2(1,\tau)$. They are in excellent agreement with the frequency responses from 5T ROM AUTO and MMS, as shown in Fig. 21. Fig. 24 (a) and Fig. 24 (b) characterize the left unstable branch end point; for frequencies to the left of the endpoint, regardless of initial amplitude, the deflections settle to the left stable branch, while for an initial amplitude greater than the endpoint and higher frequency, the deflection goes to pull-in. Fig. 24 (c) occurs at a frequency between that of the unstable endpoint and saddle-node bifurcation; since the initial amplitude is below the unstable branch, the deflection settles to a point on the left stable branch. Fig. 24 (d) characterizes the behavior in between the saddle-node bifurcation and the right branch endpoint; for any initial amplitude, the deflection will tend to pull-in behavior.

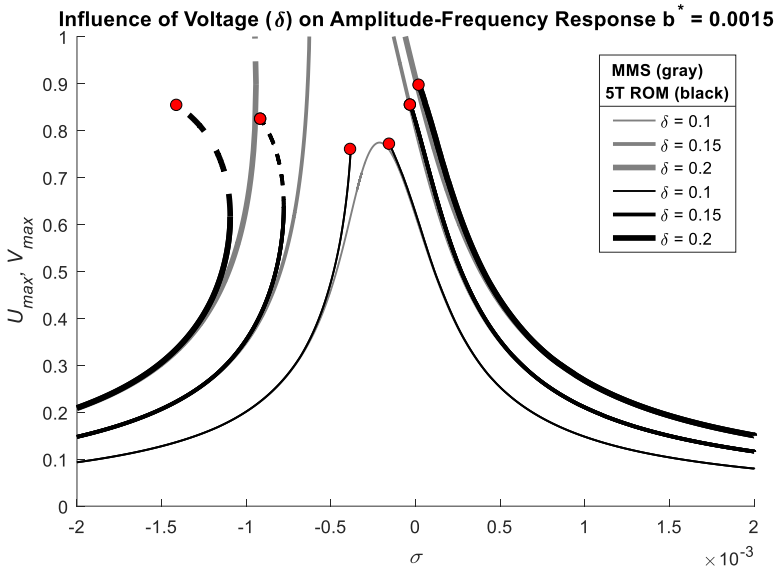

Fig. 25. Effect of applied voltage, δ, on frequency response, MMS and ROM AUTO

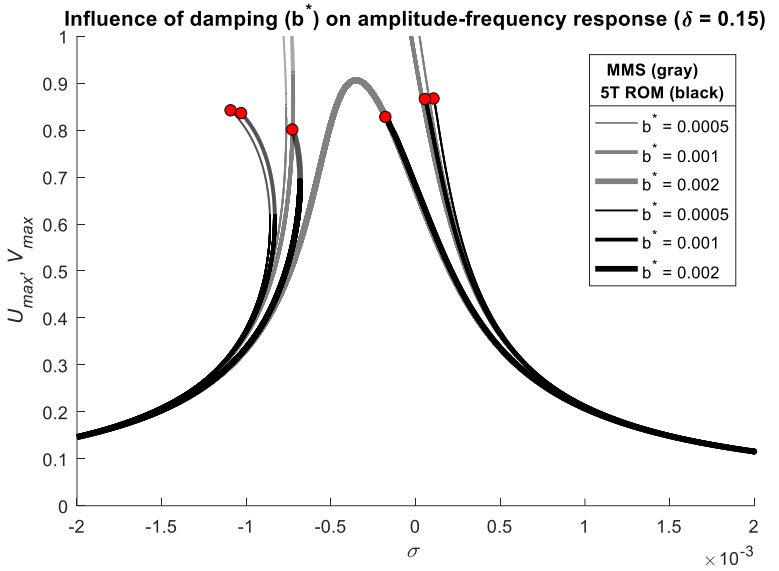

Fig. 26. Effect of dimensionless damping, *b**, on frequency response, MMS and ROM AUTO

Fig. 25 shows the effect of the voltage parameter on the frequency response. One can observe that if the voltage parameter is small the system has a linear behavior. As the voltage parameter increases the system experiences a nonlinear behavior with softening effect. The frequency of the saddle-node bifurcation point is shifted to lower frequencies while its amplitude is not significantly affected. Also, the unstable branch endpoint before pull-in is reached is shifted to lower frequencies.

Fig. 26 illustrates the effect of the damping parameter on the response. Small damping results into a nonlinear behavior of the system. As the damping increases the saddle-node bifurcation point is shifted to higher frequencies and amplitudes and the unstable branch endpoint is shifted to lower frequencies. If the damping is large enough, then the branches collapse onto each other resulting only one branch and a linear behavior of the system, with no pull-in phenomenon.

6.4 PRIMARY RESONANCE – VOLTAGE RESPONSE (COAXIAL)

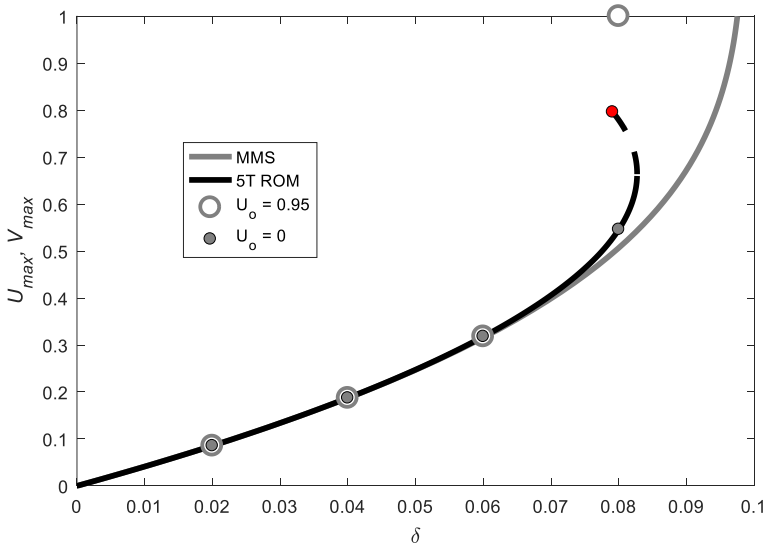

Fig. 27. Amplitude-voltage response, primary resonance, using five terms (5T) ROM and MMS, $b^* = 0.001$, $\sigma = -0.0004$

Fig. 27 shows the amplitude–voltage response of five terms reduced order model (5T ROM) in comparison with MMS. This response is a bifurcation diagram. The steady-state solutions response shown consists of two branches, a stable branch shown as solid line, and unstable branch shown as dashed line. Starting from rest at equilibrium position, as the AC voltage is increased at constant frequency, the deflection of the DWCNT increases until it reaches the saddle-node bifurcation point, where the system loses stability and jumps to pull-in (contact with the ground plate). The unstable solutions located on dashed branch are saddle points. In the voltage range of unstable branch, the amplitude decreases and settles to the corresponding (same voltage) low amplitude on the stable branch if the initial amplitude is below the dashed line, and increases to pull-in if the initial amplitude is above the dashed line. The branch solution shown in gray is the response using MMS. As can be noticed, the response from using 5T ROM and MMS are in agreement for amplitudes below 0.4 of the gap. This is due to MMS being limited to weak nonlinearities, thus underestimating the nonlinear behavior of the system at high amplitudes. MMS fails to predict the saddle-node bifurcation point and the pull-in phenomenon for large initial amplitudes, which can occur for large enough values of voltage.

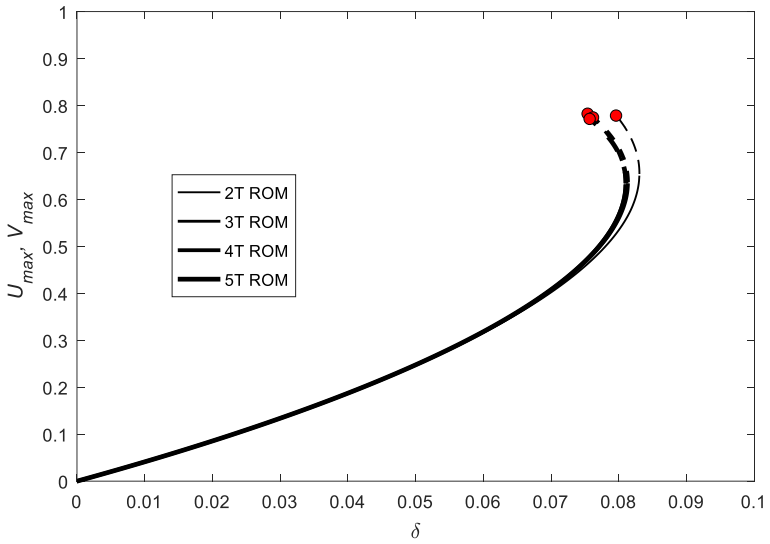

Fig. 28. ROM AUTO convergence of the amplitude-voltage response for DWCNT resonator using two terms (2T ROM), three terms (3T ROM), …, and five terms (5T ROM). AC frequency near-half natural frequency. b^* = 0.001, σ = -0.0004

Fig. 28 illustrates the convergence of the ROM method. Using numerical simulation with AUTO-07P, the number of terms considered is between two and five. One can see that the difference between the terms is only at higher amplitudes. The convergence of solutions is apparent on the unstable branch and saddle-node bifurcation point, which shifts to lower frequencies. For this case, there is no need to check for higher terms above 5T ROM since five terms is shown to be appropriate for solutions. Two terms, as in all other cases, is insufficient for higher amplitude approximation.

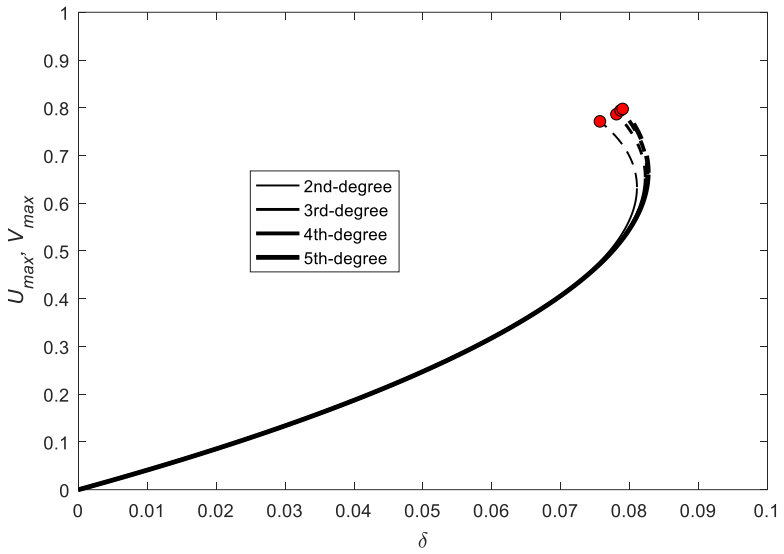

Fig. 29. ROM AUTO Taylor denominator convergence of the amplitude-voltage response for DWCNT resonator using five terms (5T ROM). AC frequency near-half natural frequency. b^* = 0.001, σ = -0.0004

Fig. 29 shows the solution convergence to increasing the degree of the Taylor polynomial in the denominator for 5T ROM. Similar to the term convergence shown in Fig. 28, a numerical solution convergence may be seen in the fifth degree of the electrostatic force (polynomial) in the denominator, with an excellent approximation of higher amplitudes. One can observe the increasing the Taylor polynomial terms shifts the unstable branch and bifurcation point to higher amplitudes.

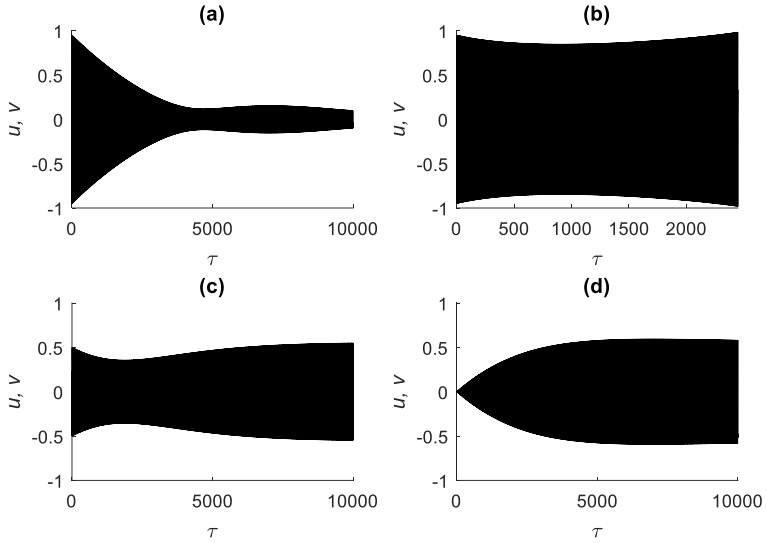

Fig. 30. Time response using 5T ROM for DWCNT resonator for AC frequency near-half natural frequency; b^* = 0.001, σ = -0.0004, (a) Initial amplitude U_0 = 0.95, δ = 0.02, (b) Initial amplitude U_0 = 0.95, δ = 0.08, (c) Initial amplitude U_0 = 0.5, δ = 0.08, (d) Initial amplitude U_0 = 0, δ = 0.08

Figs. 30 (a)-(d) show time responses using 5T ROM for b^* = 0.001 and σ = -0.0004 considering various initial amplitudes and values of voltage, where $u = w_1(1,\tau)$ and $v = w_2(1,\tau)$. They are in excellent agreement with the frequency responses from 5T ROM AUTO and MMS, as shown in Fig. 27. Fig. 30 (a) and Fig. 30 (b) characterize the left unstable branch end point; for voltages to the left of the endpoint, regardless of initial amplitude, the deflections settle to the stable branch, while for an initial amplitude greater than the endpoint and higher voltage, the deflection goes to pull-in. Fig. 30 (c) occurs at a voltage between that of the unstable endpoint and saddle-node bifurcation; since the initial amplitude is below the unstable branch, the deflection settles to a point on the stable branch. Fig. 30 (d) typifies the deflection behavior for voltages below that of the saddle-node bifurcation, where the steady-state amplitude will settle on the stable branch.

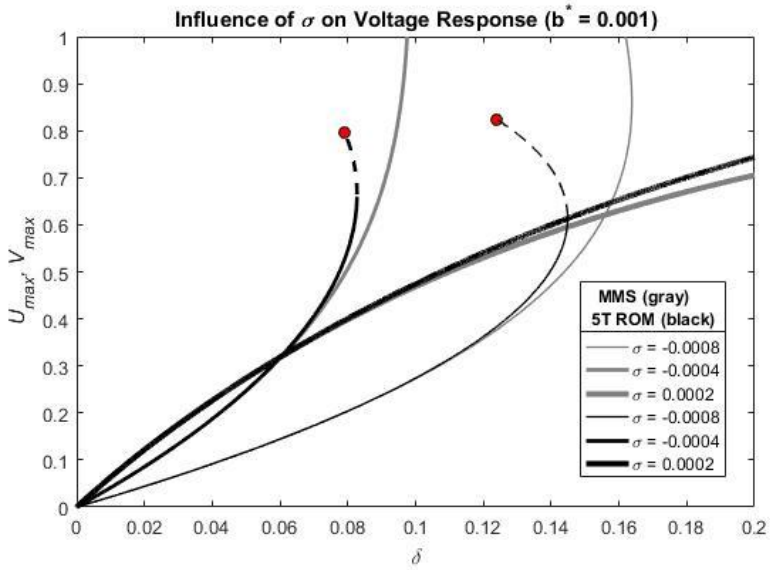

Fig. 31. Effect of detuning frequency, σ, on voltage response, MMS and ROM AUTO

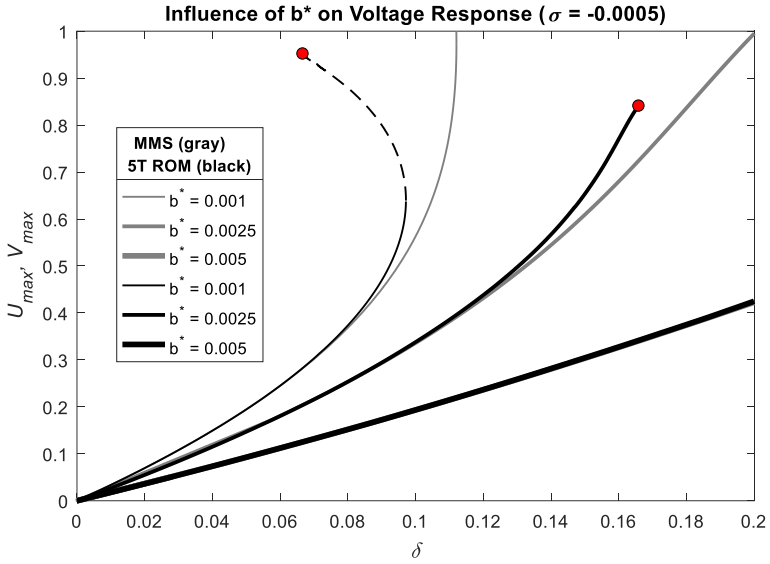

Fig. 32. Effect of dimensionless damping, *b**, on voltage response, MMS and ROM AUTO

Fig. 31 shows the influence of the detuning frequency on the voltage response of the system for three cases of frequency detuning parameter using 5T ROM and MMS. One can notice that as the frequency increases, the plate goes from a nonlinear behavior to a linear behavior. For $\sigma = 0.0002$ and higher, the DWCNT no longer experiences a bifurcation point or pull-in instability. The results from MMS exhibit the same behavior. Results from MMS and 5T ROM are identical for low amplitudes. However, MMS fails to predict the nonlinear behavior and saddle-node bifurcation at amplitudes larger than 0.4 of the gap.

Fig. 32 shows the effect of the dimensionless damping parameter on the voltage–amplitude response. Starting from a low damping coefficient of $b^* = 0.001$, as the damping parameter increases, the curves for the response of the system shift from exhibiting nonlinear behavior to linear behavior. Also, a larger voltage is required to achieve the same amplitude of vibration if large damping is present. The voltage required to reach the bifurcation point, and therefore pull-in, increases as the damping of the system increases. Lastly, pull-in instability is not present for large enough values of damping. MMS is in perfect agreement with the results from 5T ROM for low amplitudes.

CHAPTER VII

DISCUSSIONS AND CONCLUSIONS

Modal coordinates have been found using undamped DWCNT to include linear intertube van der Waals forces. Two modes of vibration resulted, coaxial and noncoaxial. This work predicted the effects voltage, detuning frequency, damping on amplitude-frequency and amplitude voltage of coaxial parametric and primary resonance of cantilever DWCNTs. Five ROMs using one through five modes of vibration were developed and used. All ROMs were expressed in terms of modal coordinates of the DWCNT. In addition, the influence of the strongly nonlinear van der Waals coefficient is presented in the amplitude-frequency response of primary resonance. The coaxial mode of vibration was investigated. The ROM using one mode of vibration was solved using the method of multiple scales in order to obtain the amplitude-frequency response. All other ROMs using one through five modes of vibration were solved either through numerical integration in Matlab in order to obtain time responses [20-22, 29, 38], or using AUTO-07P, a software package for continuation and bifurcation, in order to obtain the amplitude-frequency response. All methods are in agreement for amplitudes lower than 0.4 of the gap. For larger amplitudes, only ROM using five modes of vibration predicts accurately the behavior of the DWCNT. Increasing voltage and/or decreasing damping results in a larger range of frequencies for which pull-in occurs.

The applicability of Euler-Bernoulli beam modelling over molecular dynamics (MD) methodology and nonlocal continuum mechanics (small-scale effect) has been comprehensibly

discussed in the study of electrostatically actuated single-walled carbon nanotubes [2]. It has been shown that the small-scale effect does not have a significant influence on the fundamental frequencies of long slender carbon nanotubes [2]. A model limitation is that this investigation does not account for thermal vibrations that arise from an axial load induced by thermal expansion [39]. MD simulations and/or other experimental work is needed to validate the analytical work presented in this thesis.

REFERENCES

[1] Monthioux, M., Kuznetsov, V. L., 2006, "Who should be given the credit for the discovery of carbon nanotubes?" CARBON **44**.

[2] Caruntu, D.I., Luo, L., 2014, "Frequency response of primary resonance of electrostatically actuated CNT cantilevers," Nonlinear Dynamics **78**, 1827-1837.

[3] Santiago, E. V., Lopez, S. H., Camacho Lopez, M. A., Contreras, D. R., Farias-Mancilla, R., Flores-Gallardo, S. G., Hernandez-Escobar, C. A., and Zaragoza-Contreras, E. A., 2016, "Optical Properties of Carbon Nanostructures Produced by Laser Irradiation on Chemically Modified Multi-Walled Carbon Nanot ubes," Opt. Laser Technol., **84**, pp. 53–58.

[4] Azooz, S. M., Ahmed, M. H. M., Ahmad, F., Hamida, B. A., Khan, S., Ahmad, H., and Harun, S. W., 2015, "Passively Q-Switched Fiber Lasers Using a Multi-Walled Carbon Nanotube Polymer Composite Based Saturable Absorber," Opt. - Int. J. Light Electron Opt., **126**(21), pp. 2950–2954.

[5] Yu, H., Zhang, L., Wang, Y., Yan, S., Sun, W., Li, J., Tsang, Y., and Lin, X., 2013, "Sub-100ns Solid-State Laser Q-Switched with Double Wall Carbon Nanotubes," Opt. Commun., **306**, pp. 128–130.

[6] Sánchez-Tirado, E., Salvo, C., González-Cortés, A., Yáñez-Sedeño, P., Langa, F., and Pingarrón, J. M., 2017, "Electrochemical Immunosensor for Simultaneous Determination of Interleukin-1 Beta and Tumor Necrosis Factor Alpha in Serum and Saliva Using Dual Screen Printed Electrodes Modified with Functionalized Double–walled Carbon Nanotubes," Anal. Chim. Acta, **959**, pp. 66–73.

[7] Li, Y., Wu, T., and Yang, M., 2014, "Humidity Sensors Based on the Composite of Multi-Walled Carbon Nanotubes and Crosslinked Polyelectrolyte with Good Sensitivity and Capability of Detecting Low Humidity," Sensors Actuators, B Chem., **203**, pp. 63–70.

[8] Geng, D., Li, M., Bo, X., and Guo, L., 2016, "Molybdenum Nitride/nitrogen-Doped Multi-Walled Carbon Nanotubes Hybrid Nanocomposites as Novel Electrochemical Sensor for Detection L-Cysteine," **237**, pp. 581–590.

[9] Kiani, K., 2015, "Nanomechanical Sensors Based on Elastically Supported Double-Walled Carbon Nanotubes," Appl. Math. Comput., **270**, pp. 216–241.

[10] Lawal, A. T., 2016, “Synthesis and Utilization of Carbon Nanotubes for Fabrication of Electrochemical Biosensors,” Mater. Res. Bull., **73**, pp. 308–350.

[11] Morelos-Gómez, A., Fujishige, M., Magdalena Vega-Díaz, S., Ito, I., Fukuyo, T., Cruz-Silva, R., Tristán-López, F., Fujisawa, K., Fujimori, T., Futamura, R., Kaneko, K., Takeuchi, K., Hayashi, T., Kim, Y. A., Terrones, M., Endo, M., and Dresselhaus, M. S., 2016, “High Electrical Conductivity of Double-Walled Carbon Nanotube Fibers by Hydrogen Peroxide Treatments,” J. Mater. Chem. A, **4**(1), pp. 74–82

[12] Wang, S., Liang, X. L., Chen, Q., Yao, K., and Peng, L. M., 2007, “High-Field Electrical Transport and Breakdown Behavior of Double-Walled Carbon Nanotube Field-Effect Transistors,” Carbon N. Y., **45**(4), pp. 760–765.

[13] Dequesnes, M., Rotkin, S.V., Aluru, N.R., 2002 "Calculation of pull-in voltages for carbon nanotube based nanoelectromechanical switches." Nanotechnology, **13**, pp 120-131.

[14] Caruntu, D.I., Juarez, E., 2019, “Voltage effect on amplitude–frequency response of parametric resonance of electrostatically actuated double-walled carbon nanotube resonators,” Nonlinear Dynamics, https://doi.org/10.1007/s11071-019-05057-8.

[15] Yan, Y., Wang, W., Zhang, L., 2011, “Applied multiscale method to analysis of nonlinear vibration for double-walled carbon nanotubes,” Applied Mathematical Modelling, **35**, pp. 2279-2289

[16] Natsuki, T., Lei, X., Ni, Q., Endo, M., 2010, “Vibrational analysis of double-walled carbon nanotubes with inner and outer nanotubes of different lengths,” Physical Letters A, **374**, pp. 4684-4689

[17] Murmu, T., McCarthy, M. A., Adhikari, S., 2012, “Vibration response of double-walled carbon nanotubes subjected to an externally applied longitudinal magnetic field: A nonlocal elasticity approach,” Journal of Sound and Vibration, **331**, pp. 5069-5086

[18] Hajnayeb, A., Khadem, S. E., 2012, “Nonlinear vibration and stability analysis of double-walled carbon nanotube under electrostatic actuation,” Journal of Sound and Vibration, **331**, pp. 2443-2456

[19] RB Hudson, A Sinha Vibration of carbon nanotubes with defects: order reduction methods, Proc. R. Soc. A, **474**: 20170555, 2018

[20] Caruntu, D.I., Martinez, I., Taylor, K.N., 2013, “Voltage-Amplitude Response of Alternating Current Near Half Natural Frequency Electrostatically Actuated MEMS Resonators,” Mechanics Research Communications **52**, pp. 25– 31.

[21] Caruntu, D.I., Martinez, I., 2014, “Reduced order model of parametric resonance of electrostatically actuated MEMS cantilever resonators,” International Journal of Non-linear Mechanics, **66**, pp. 28-32

[22] Caruntu, D.I., Martinez, I., Knecht, M.W., 2013, “ROM analysis of frequency response of AC near half natural frequency electrostatically actuated MEMS cantilevers,” Journal of Computational and Nonlinear Dynamics, **8**, 031011-1 - 031011-6.

[23] Ru, C.Q., in Encyclopedia of Nanoscience and Nanotechnology, edited by H. S. Nalwa (American Scientific, Stevenson Ranch, CA, 2004), **2**, pp. 731–744.

[24] Bhiladvala, R.B., Wang, Z.J., 2004, “Effects of fluids on the Q factor and the resonance frequency of oscillating micrometer and nanometer scale beams”, Physical Review E, **69**, 036307.

[25] Xu, K.Y., Guo, X.N., 2006, "Vibration of double-walled carbon nanotube aroused by nonlinear intertube van der Waals forces," Journal of Applied Physics, **99**.

[26] Jackson J D 1998 *Classical Electrodynamics* 3rd edn (New York: Wiley)

[27] Chen, G., Bandow, S., Margine, E.R. Nisoli, C., Kolmogorov, A.N., Crespi, V. H., Gupta, R., Sumanasekera, G.U., Ijima, S., Eklund, P.C., 2013, "Chemically Doped Double-Walled Carbon Nanotubes: Cylindrical Molecular Capacitors," Physical Review Letters, **90**(25).

[28] Inman, David J. 2008 *Engineering Vibration* 3rd ed (Pearson-Prentice Hall)

[29] Caruntu, D.I, Knecht, M., 2015, “MEMS cantilever resonators under soft AC voltage of frequency near natural frequency,” Journal of Dynamic Systems, Measurement and Control, **137**, 041016-1

[30] Shampine, L. F., and Reichelt, M. W., 1997, “The MATLAB ODE Suite,” SIAM: J. Sci. Comput., **18**, pp. 1–22.

[31] Shampine, L. F., Reichelt, M. W., and Kierzenka, J. A., 1999, “Solving Index-1 DAEs in MATLAB and Simulink,” SIAM Rev., **41**(3), pp. 538–552

[32] Nayfeh, Ali H., and Dean T. Mook. *Nonlinear oscillations*. John Wiley & Sons, 2008.

[33] Nayfeh, Ali H. *Introduction to perturbation techniques.* John Wiley & Sons, 2011

[34] Nayfeh, A.H., Younis, M.I., Abdel-Rahman, E.M.: Dynamic pull-in phenomenon in MEMS resonators. Nonlinear Dyn. **48**, 153–163 (2007)

[35] Scherling, Alexander I. “Reduced-Order Reference Models for Adaptive Control of Space Structures.” *California Polytechnic State University*, 2014.

[36] Saghir, S., Younis, M.I., 2016, “An investigation of the static and dynamic behavior of electrically actuated rectangular microplates,” International Journal of Non-Linear Mechanics **85**, pp, 81-93

[37] Ouakad, H., Younis, M.I., 2014, “On using the dynamic snap-through motion of MEMS initially curved microbeams for filtering applications,” Journal of Sound and Vibration **333**, pp. 555-568

[38] Caruntu, D.I., Taylor, K.N., 2014, “Bifurcation type change of AC electrostatically actuated MEMS resonators due to DC bias,” Shock and Vibration, Article ID 542023, 9 pages

[39] Wang LF, Hu HY, “Thermal vibration of a simply supported single-walled carbon nanotube with thermal stress,” Acta Mechanica, **227**(7):1957-1967

BIOGRAPHICAL SKETCH

Ezequiel Juarez Ocanas was born in Reynosa, Tamaulipas, Mexico on May 4, 1993. He attended McAllen High School in McAllen, TX, graduating in 2012. He attended the University of Texas – Pan American, Edinburg, TX, first earning a Bachelors of Science degree in Mechanical Engineering in 2015. More recently, he has attended the University of Texas – Rio Grande Valley, Edinburg, TX, receiving a Masters of Science in Mechanical Engineering in Summer of 2019. He currently resides at 3717 Toucan Ave, McAllen, TX, 78504.